High Spectral Resolution Chirp Modulation Stimulated Raman Scattering Microscopy

Leah Frackleton

Thesis submitted to the University of Ottawa in partial fulfillment of the requirements for the degree of Master of Science, Physics

Department of Physics
Faculty of Science
University of Ottawa

Prof. Albert Stolow, Dr. Adrian Pegoraro

Abstract

Stimulated Raman scattering (SRS) microscopy enables rapid, chemical-specific, label-free imaging and is a powerful technique for bioimaging and material characterization. In spectral focusing SRS, the two input laser pulses are linearly chirped and delay-scanned, providing rapid tunability while preserving Raman spectral resolution. Conventional linear modulation-transfer detection schemes commonly used in SRS, however, can be challenged by non-Raman backgrounds. Leveraging the quadratic phase control inherent to spectral focusing SRS enables Chirp modulation (CM)-SRS, a modulation transfer technique based upon modulating only the sign of the linear chirp. CM-SRS cancels all non-Raman signals while retaining a quantitative, highly sensitive Raman response. Motivated by these advantages, we designed and implemented an updated CM-SRS setup optimized for maximal background subtraction. Achieving both high spectral resolution and quality chirp matching in spectral focusing CM-SRS requires fine control over the pulse chirps at the microscope sample plane. To this end, we developed Fringe-averaged collinear Frequency-resolved optical gating (FRACOL-FROG), a robust method for *in situ* characterization of the input laser fields. Together, these advances position our CM-SRS microscopy system to deliver high-resolution, background-free, chemical-specific, and high-sensitivity measurements across a range of important samples previously challenged by background signals.

Acknowledgements

I would like to thank many people for their support throughout my time at the University of Ottawa and as a member of Prof. Albert Stolow's group. Firstly, thanks to my family for their love and encouragement, and to my cats Snowshoes and Zoe. I would like to thank Simaya, whom I met through my undergrad in physics. She has encouraged me to step out of my box, take new opportunities and be engaged in the physics community. Merci aussi à mes autres amis du B.Sc en physique, vous me manquez. I have met many great people in the uOttawa physics community, including from the Physics Society, the Optica-SPIE Joint Student chapter, and the Throwdinger Cats/Bally Exclusion dodgeball teams, all of whom have made school more enjoyable. I also thank my friends from my time at the Max-Planck Institute for the Science of Light and from the Optica Women Scholars whom I can look forward to seeing at future meetings and conferences throughout my career.

Thank you to Albert for taking a chance on me as a first-year undergrad student and for his continued support throughout the years. Thanks to Adrian Pegoraro for teaching me, for the countless nights spent helping with writing, and even for letting me follow him around this year at my first major conference. Thank you to Siddarth Shivkumar, for the help and advice, even months after moving to another continent, and for being the other half of team FROG. I would like to thank Mehdi Alizadeh for his support and for keeping me fuelled with chocolate time, and Hannah Gallop for joining me in a lot of random sports and activities. Thank you to the rest of the members of the Stolow group, past and present, for helping to create a fun work environment, for the daily park lunches, for helping in decorating ARC for all holidays and birthdays, and for still finding my FROG jokes entertaining. I have received support from many people throughout these years, thank you to everyone.

I thank the Optica Women Scholars program, which along with financial support, has provided me with unique opportunities and a great international community of peers and colleagues. I also acknowledge funding from the Ontario Graduate Scholarship program. The template for this thesis was written by Nicholas Sorensen.

Author Contributions

The research in this thesis was made possible by contributions from many collaborators. My co-supervisors, Albert Stolow and Adrian Pegoraro, provided guidance and feedback throughout the research presented in this work. Adrian, Albert, Siddarth (Sid) Shivkumar and Mehdi Alizadeh provided valuable technical feedback during the writing of this thesis.

Part I: I originally implemented a collinear FROG (cFROG) system with help from Adrian and Alexander (Alex) Harper. When interferometric instabilities proved too great an obstacle in implementing cFROG, Albert suggested interferometric path length dithering. The first successful prototype used a hairdryer borrowed from his partner Karina. This idea evolved into FRACOL-FROG with a piezo-driven retroreflector, first implemented by Malcolm Latorre and Sid. Sid and I closely collaborated on characterizing this system, learning the FROG algorithm, and writing the FRACOL-FROG paper, often tag-teaming measurements, preprocessing, running the FROG retrieval and plotting. Daniel J. Kane and Keith A. Wernsing of Mesa Photonics also provided valuable insights on the FROG retrieval algorithm. Sid developed simulations to support the theory, with feedback from Adrian and myself. The manuscript was mainly written by Sid and myself, with input from Adrian, Albert, Malcolm and Alex. All Stolow group members contributed to the all-important naming of the technique.

Part II: I designed the second-generation CM-SRS system in close collaboration with Sid and Adrian, with input from Albert, Alex and Mehdi. Sid and I collaborated on the initial building of the system. I was responsible for full system alignment and chirp-matching of the grating stretchers. Mehdi and Hannah Gallop assisted with coupling the beam into the microscope. Albert and Adrian helped diagnose vertical spatial chirp in the system, which prompted a small redesign. Adrian and Sid taught me the daily calibration procedure. Adrian, Mehdi, Malcolm and Alex helped configure the system for SRS measurements. Adrian provided the deconvolution simulation code.

Contents

List of Figures

List of Abbreviations

β-BBO Beta Barium Borate 33, 35

AI artificial intelligence 77, 78

AM Amplitude-modulation 3, 4, 6, 7, 51–59, 62, 73, 75, 77

bFROG baseband FROG 25

CARS coherent anti-Stokes Raman scattering 2, 51

CEP carrier-envelope phase 25

cFROG collinear FROG 22–26, 29–31, 33, 36–43, 46, 81

CM Chirp-modulation 7, 21, 47, 49–51, 53–60, 62, 63, 65, 68, 70–77, 79–82

CRM Coherent Raman microscopy 2, 6, 7, 21, 22, 32, 47, 51

DMSO dimethyl sulfoxide 58, 73, 75

FFT Fast Fourier transform 15, 16

FRACOL-FROG Fringe-averaged collinear FROG 7, 9, 25–27, 30–47, 62, 68, 69, 76, 81, 82

FROG Frequency-resolved optical gating 7, 9, 11–19, 21–26, 28, 30–32, 35–47, 81, 82

FWHM full width at half maximum 11, 17, 30–32, 41–45, 70

GVD group-velocity dispersion 65

H&E hematoxylin and eosin 77–79

HWP half-wave plate 33, 62–64, 72

ISRS impulsive SRS 6

NA Numerical aperture 23, 34, 35, 46, 65

NLO nonlinear optics 9

PBS polarizing beam splitter 33, 62, 64

PCGP Principal components generalized projections 17, 36

PG FROG Polarization-gate FROG 13

PMT photomultiplier tube 65, 69, 76

QWP quarter-wave plate 63, 64

RANA Retrieved-Amplitude N-grid Algorithmic 18, 19, 36

SHG Second harmonic generation 11–16, 18, 24, 26, 29–33, 35, 37, 39, 46, 82

SRH Stimulated Raman histology 77–79

SRL Stimulated Raman loss 3, 4, 51

SRS Stimulated Raman scattering 2–7, 21, 47, 49–60, 62, 63, 65, 68, 73–82

TBP time-bandwidth product 16, 17, 19

THG Third harmonic generation 13, 24

1

Introduction

Optical microscopy is a powerful technique for bioimaging and material characterization. Fluorescence microscopy, one of the most widely used modalities, typically relies on labeling different regions with specific fluorophores to achieve contrast. Its strengths lie in its single-molecule sensitivity, rapid imaging capabilities, and compatibility with super-resolution imaging techniques. However, fluorescent labels may potentially modify cellular behaviour and, in certain material samples, cannot be applied [1, 2]. In many cases, there

is a need for label-free techniques which make use of intrinsic contrast. An example of such a technique is spontaneous Raman scattering which probes molecular vibrations by measuring the scattered light from a system, making it both chemical-specific and label-free. Unfortunately, spontaneous Raman scattering is a very weak process, plagued by slow imaging speeds and can be overwhelmed by background fluorescence [2, 3]. Near-field Raman techniques improve sensitivity through plasmonic enhancement factors but require close, potentially disruptive, contact with the sample and are not easily applied to complex three-dimensional materials [2, 4]. Resonance Raman scattering, where the input laser is tuned near an electronic resonance, results in orders of magnitude Raman enhancement but often comes with large fluorescence backgrounds and molecular photobleaching [2, 5].

Coherent Raman microscopy (CRM) is a nonlinear optical, vibrationally resonant counterpart of spontaneous Raman scattering, which, due to its stimulated nature, is orders of magnitude more sensitive [6, 7]. An important variant, Stimulated Raman scattering (SRS), is typically based on two input laser fields (called Pump and Stokes) whose frequency difference is tuned to match vibrational Raman resonances of the target molecules, as seen in Fig. 1.1. For condensed targets, the enhanced sensitivity of SRS allows for video-rate imaging [2, 8, 9]. SRS has linear dependence on concentration and spectral line shapes closely resembling those of spontaneous Raman spectra [10]. It is also free of the non-resonant four-wave mixing background that is present in coherent anti-Stokes Raman scattering (CARS), another important CRM modality [11].

In SRS, when the frequency difference between the pump and Stokes is tuned to a vibrational resonance, there is a transfer of energy between the beams leading to a loss in

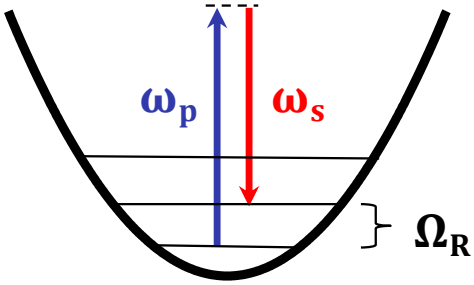

Figure 1.1: **Excitation of vibrational mode in SRS:** Two input laser fields, the pump (ω_p) and Stokes (ω_s), drive a vibrational Raman resonance of frequency $\Omega_R = \omega_p - \omega_s$.

the pump beam and a gain in the Stokes beam. This variation in signal is measurable but is tiny compared to the total laser power [11, 12]. For enhanced detection of this Raman resonant energy transfer, modulation transfer schemes with lock-in amplifier detection are typically applied. Many linear optical modulation techniques developed for the telecommunication industry [13] have been applied to SRS [11, 14, 15], the simplest of which being Amplitude-modulation (AM) [12].

In AM-SRS, the amplitude of one input laser is modulated on and off at high (typically MHz) frequencies, and the other (unmodulated) laser is detected using a photodiode [11, 12]. When the input lasers' frequency difference is tuned to a Raman resonance, there will be a transfer of energy from one field to the other. When the modulated beam is blocked, there will be no energy transfer and the full power of the unmodulated beam remains unchanged. In Stimulated Raman loss (SRL), the Stokes beam is modulated and a loss in the pump beam is detected, as seen in Fig. 1.2 [12]. In a typical optical microscopy experiment, the difference in signal caused by the energy transfer is quite

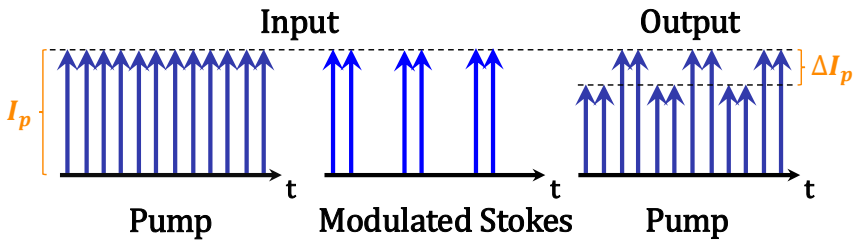

Figure 1.2: **Amplitude modulation for SRL:** In SRL, the loss in energy caused by the Raman excitation is detected. To facilitate this, the Stokes beam is modulated at a known repetition rate, which will cause a loss (ΔI_P) in the pump beam at this same frequency.

small ($\Delta I_p/I_p < 10^{-4}$). However, because the intensity variation has a repetition rate that matches the known AM frequency, it is possible to extract this signal using a lock-in amplifier [12].

1.1 Spectral focusing

The goal in SRS microscopy is to probe specific Raman resonances in order to achieve chemical contrast. Thus, it must be possible to tune the frequency difference between the two input fields. Additionally, the spectral resolution should be high enough that it is possible to distinguish between different Raman resonances. This is determined by the Raman spectral resolution, which is defined as the bandwidth of the detected difference frequencies. The spectral resolution is set by the bandwidth of the lasers used for excitation. If one were to use narrow-band picosecond pulses, as in Fig. 1.3(a), there would be high Raman spectral resolution for the given frequency difference. In principle, even longer pulses would offer even higher spectral resolution. However, nonlinear optical responses

such as SRS require pulses with high peak intensities for efficient signal generation, so there is a practical limit to how long a pulse can be used [16], favouring short pulses. A practical limitation when using picosecond pulses is that tuning between wavelengths can be a time-consuming process. As an alternative to picosecond pulses, it is possible to use two broadband femtosecond pulses, as the frequency difference will yield a broad bandwidth, as seen in Fig. 1.3(b). However, since the spectral resolution is poor, many Raman modes will be probed simultaneously [16]. It should be noted that this poor spectral

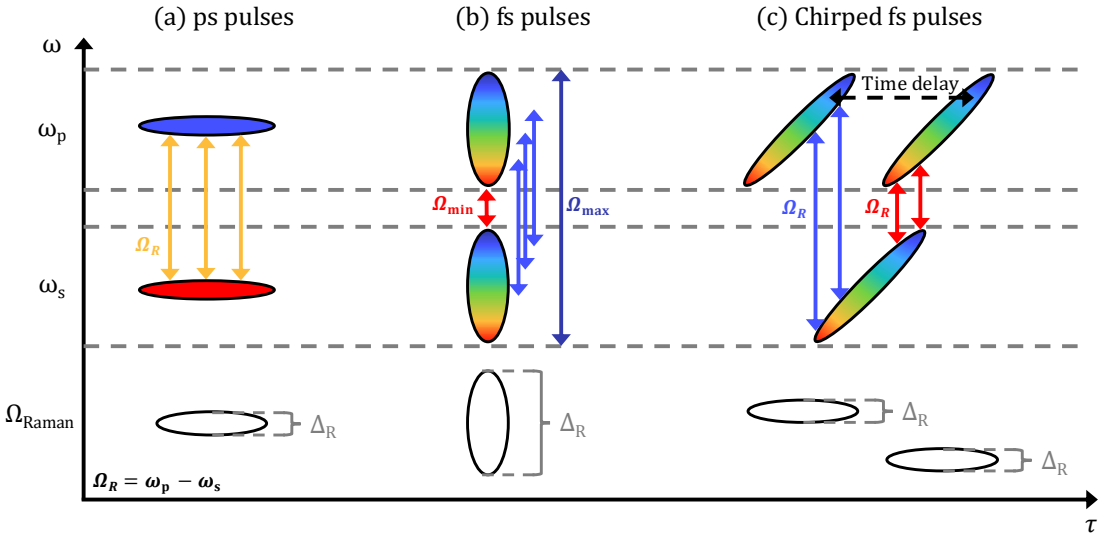

Figure 1.3: **Spectral focusing SRS:** Raman resolution Δ_R as a function of input laser fields. (a): Narrowband picosecond pulses will have a narrow Raman resolution, but at a cost of slow tunability and much lower nonlinear optical signals. (b): Femtosecond pulses will have a broad tuning range and much higher signals, but with poor Raman resolution. (c): Chirped femtosecond pulses can give both narrow Raman resolution and high tunability in a configuration known as spectral focusing [17].

resolution is only a problem when measuring the instantaneous response. If a time-delayed probe pulse is used, it is possible to measure the decay of the excited Raman modes in a

pump-probe arrangement. By Fourier transforming this temporal decay, it is possible to recover the Raman spectrum. This is known as impulsive SRS (ISRS) and can provide high quality Raman spectra [18]. However, the excitation frequency range is a function of the bandwidth of the pump beam, making ISRS generally better suited to Raman imaging in a lower wavenumber regime ($< 400\ cm^{-1}$) [18, 19].

A technique that allows for both rapid tunability and high Raman spectral resolution is known as spectral focusing [16, 20, 21]. In this technique, the frequency components of the two broadband femtosecond input fields are spread linearly in time (chirped) so that their instantaneous frequency difference is narrow-band, as seen in Fig. 1.3(c). A linear frequency chirp is equivalent to a quadratic variation in spectral phase, since frequency is by definition the time-derivative of phase. To change the probed Raman resonance, the relative temporal delay between the pump and Stokes is varied, changing the instantaneous frequency difference and thus mapping a given delay to a specific Raman shift. This method of SRS allows for rapid tunability with high chemical specificity via Raman resonance [16].

1.2 Overview

Despite its many successes, spectral focusing AM-SRS also has important limitations. Ideal resolution in spectral focusing requires the pump and Stokes chirps (quadratic phases) to be perfectly linear and matched in value, which is often not the case in practice. Part I of this thesis examines how mismatched chirps and higher order (cubic, quartic) phase variations can degrade Raman resolution in spectral focusing CRM and thus the need for

measuring these higher-order phases (nonlinear chirps) at the microscope focus. This in turn requires advanced optical tools such as Frequency-resolved optical gating (FROG), which will be introduced in Chapter 2. Chapter 3 presents our laser pulse characterization technique, Fringe-averaged collinear FROG (FRACOL-FROG) [22], which is specifically suitable for use in CRM applications.

A second limitation of spectral focusing AM-SRS is that it is not background-free. Depending on the sample, non-Raman background signals, such as those due to nonlinear scattering and nonlinear absorption, can overwhelm the Raman response and compromise chemical specificity. Our group recently developed a powerful new CRM modality called Chirp-modulation (CM)-SRS [10, 23] that essentially removes all non-Raman background signals. Part II of this thesis presents the theory of CM-SRS microscopy (Chapter 4), followed by a description of an improved experimental implementation and a consideration of prospective applications (Chapter 5).

Part I

Characterization of ultrashort pulses in nonlinear microscopy

The electric fields of optical frequency ultrashort laser pulses are difficult to characterize using traditional means such as oscilloscopes because their PHz frequencies vastly exceeds the bandwidth of the fastest electronics (GHz). In general, measuring an event requires a probe of comparable or shorter duration, analogous to needing to use a caliper and not a meter stick to accurately measure the thickness of a sheet of paper [24]. To address this issue, several laser pulse characterization techniques have been developed which use a laser pulse to measure itself, known as self-referencing measurement techniques. A common self-referencing technique is intensity autocorrelation, which uses nonlinear optics (NLO) in an interferometer system to mix two copies of a laser pulse to obtain the field intensity as a function of time, giving information such as the pulse duration [24, 25]. While still useful, intensity autocorrelation cannot yield information about the spectral phase of a pulse. FROG was invented to address this issue and yields information on both the intensity and phase (temporal and spectral) of a pulse [24]. Accurate laser pulse characterization is useful in many applications, including in nonlinear microscopy, and we developed a modified FROG system optimized to the needs of *in situ* (i.e. measured at the focus of an objective lens) characterization for nonlinear microscopy.

Chapter 2 will give an overview of FROG and the FROG algorithm. Chapter 3 will discuss why we implemented a FROG system in our nonlinear microscopy lab, and present our technique FRACOL-FROG, published in 2024 [22]. For more background information on FROG and ultrashort laser pulse characterization, recommended reading is the FROG textbook by R. Trebino [24] as it is well written, easy to understand and entertaining.

2

Frequency-resolved optical gating

We consider here the mathematical description of a short laser pulse. The temporal complex amplitude of a laser field may be written as [24]:

$$E(t) \equiv \sqrt{I(t)} \exp\left[-i\phi(t)\right], \tag{2.1}$$

and is dependent on both the temporal intensity $I(t)$ and the temporal phase $\phi(t)$. This field can also be expressed in the frequency domain as [24]:

$$\tilde{E}(\omega) = \sqrt{S(\omega)} \exp\left[-i\phi(\omega)\right], \tag{2.2}$$

with $S(\omega)$ the spectrum and $\phi(\omega)$ the spectral phase. $E(t)$ and $\tilde{E}(\omega)$ are related by Fourier transform. To fully characterize a laser pulse, information is required on both the intensity (or spectrum) and the temporal (or spectral) phase [24].

To obtain the pulse spectrum $S(\omega)$, a spectrometer is typically used [24]. To obtain temporal information from $I(t)$, such as the pulse duration, a common technique to use is Second harmonic generation (SHG) intensity autocorrelation. SHG autocorrelation is defined as [24, 26]:

$$A^{SHG}(\tau) = \int_{-\infty}^{\infty} I(t+\tau) I(t) \mathrm{d}t, \tag{2.3}$$

with τ representing the relative delay between the two pulses of the self-referencing technique. If assumptions are made about the pulse shape, then it is possible to obtain the temporal duration from the full width at half maximum (FWHM) of the measurement. However, neither of these measurements yield detailed information on the pulse phases [24].

FROG spectrally resolves an intensity autocorrelation to obtain the intensity I_{FROG} of

the field as a function of relative delay τ and frequency ω:

$$I_{FROG}(\omega, \tau) = \left| \int_{-\infty}^{\infty} E_{sig}(t, \tau) \exp(-i\omega t) \mathrm{d}t \right|^2, \tag{2.4}$$

with E_{sig} representing the pulse field for the given FROG geometry [26]. In the case of SHG FROG, $E_{sig} = E(t)E(t-\tau)$ [24, 26]. Eq. 2.4 is a form of the 2D phase-retrieval problem commonly found in imaging, where the measured intensity is the squared magnitude of the Fourier transform of the desired quantity [24, 26, 27]. In FROG, this inversion is reliably solvable because the mathematical form of $E_{sig}(t, \tau)$ is known. The FROG algorithm solves this 2D phase-retrieval problem, allowing it to retrieve the relative phase of the measured pulse. This distinguishes it from an intensity autocorrelation, which is a form of 1D phase-retrieval problem that has no unique solution, precluding information on the relative phases of the laser pulse [24, 26].

2.1 Implementation

The general implementation of FROG involves an interferometer-like setup where one laser pulse is split into two replicas, with one copy varied in time delay, and then the two copies mixed in a nonlinear medium. The resulting FROG signal is recorded in a spectrometer as a function of relative time delay and frequency. Typically, a noncollinear mixing geometry is used to facilitate spatial separation of the FROG signal from the other beams, as depicted in Fig. 2.1 for SHG FROG [24].

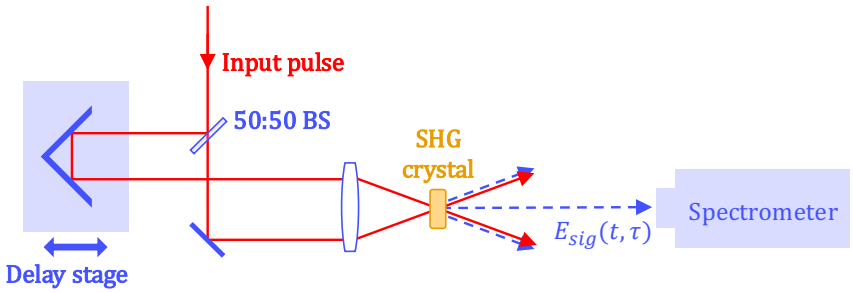

Figure 2.1: **Typical SHG FROG setup:** SHG FROG typically uses a noncollinear geometry as depicted here. In this configuration, the two beam copies are focused at opposite input angles onto a SHG crystal, generating an isolated signal field $E_{sig}(t,\tau)$ in the middle, which is then collected by a spectrometer [24]. BS = beam splitter.

SHG FROG is widely used owing to its high sensitivity and simplicity compared to other FROG modalities [24, 28]. Other forms of FROG include Third harmonic generation (THG) FROG, Polarization-gate FROG (PG FROG), and others, with the optimal choice of modality depending on the application [24]. For our application, we employed SHG FROG, as discussed below.

When collecting the FROG trace, it is crucial that the trace is fully measured in time and frequency. Any cropping would remove information about the FROG trace and prevent accurate pulse retrieval [24]. After acquisition, the 2D spectrogram is preprocessed (described below in Subsection 2.2.1) and then passed to the FROG retrieval algorithm, which solves for the input pulse [24]. This overall workflow is shown in the block diagram in Fig. 2.2.

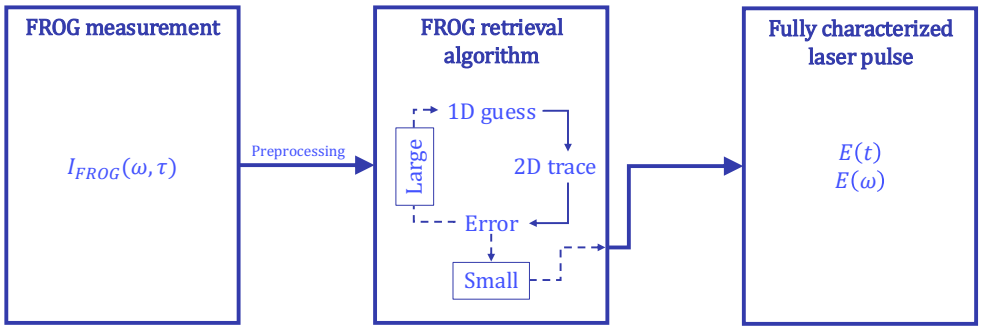

Figure 2.2: **Typical FROG workflow:** The FROG method can be divided in two main components: first the data acquisition of the spectrogram $I_{FROG}(\omega, \tau)$, and then the iterative retrieval algorithm, which solves for the electric fields $E(t)$ and $E(\omega)$.

2.2 Retrieval algorithm

A key component of FROG is the retrieval algorithm, which reconstructs the unknown input field from the measured FROG trace. The discussion here focuses on SHG FROG, but the principles generally will apply to any FROG modality. One main advantage of SHG FROG owing to its widespread use is that many reliable implementations of the SHG FROG algorithm are publicly available, making custom programming unnecessary.

One important quantity in FROG retrieval is the G error, a measure of algorithm convergence. The G error measures the difference between the experimental trace and the reconstructed trace:

$$G^{(k)} = \sqrt{\frac{1}{N^2} \sum_{i,j=1}^{N} \left| I_{FROG}(\omega_i, \tau_j) - \mu I^{(k)}_{FROG}(\omega_i, \tau_j) \right|^2}, \tag{2.5}$$

with N defined by the grid size $N \times N$ and representing the number of rows/columns, I_{FROG} the experimental trace, $I_{FROG}^{(k)}$ the reconstructed trace of the k-th iteration, and μ representing a scaling factor. Because the G error depends on grid size, both should be reported together. Typical acceptable G error values for SHG FROG retrieval on a 128×128 grid are < 0.005 [24].

2.2.1 Preprocessing

Before being passed to the FROG retrieval algorithm, the measured trace must undergo preprocessing to be compatible with Fast Fourier transform (FFT) and the iterative nature of the algorithm [24]. These steps are discussed in detail in chapters 9 and 10 of the FROG textbook [24], with the main points summarized here.

Because FROG assumes a pulse of finite temporal duration and spectral bandwidth, the measured trace must reach zero at the perimeter of the scan. Residual background at large delay can add high-frequency noise into the pulse wings. As such, the first preprocessing step of the FROG trace is background subtraction [24]. One method is to subtract the average of the columns on the edges of the trace from every pixel. To further dampen residual background, the next step is corner suppression, which involves multiplying the trace by a radially symmetric function that is ≈ 1 near the centre and smoothly approaches 0 near the edges of the trace, such as a super Gaussian. This reduces additive noise on the edges of the trace without significantly altering the centre [24]. Another method of attenuating high-frequency noise in the trace is low-pass Fourier filtering [24]. In our case,

this will be required regardless for our chosen FROG geometry, as further discussed in Chapter 3.

It is characteristic of SHG FROG to be symmetric in time, so another preprocessing step is to calibrate the delay axis to centre the trace around $\tau = 0$. The FROG algorithm also expects a grid with evenly spaced time and frequency steps [24]. Because many spectrometers do not give data linear in frequency and instead typically report wavelength, the next step is to interpolate the raw FROG grid onto a grid of uniform step size in both time and frequency.

The next step involves interpolating the data onto a FROG grid that satisfies two main criteria: (i) it must be of size $2^M \times 2^M, M \in \mathbb{N}$, and (ii) the step size of the delay axis must be the Fourier transform of the frequency axis step size. Both are required to be compatible with FFTs [24]. If upon interpolation the measured FROG trace approaches an edge along either axis, typically causing the appearance of an elliptical trace, the grid step size will need to be adjusted. To do so, one must first change the step size so that the trace is nearly equally spaced in both axes, keeping in mind that increasing the step size in τ will decrease the step size in ω. Next, if there is not enough zero-padding around the FROG trace, one should increase the grid size by a factor of 2. Use the smallest possible grid size for a given pulse, as larger grids will take longer to converge. Note that as pulse time-bandwidth product (TBP) increases, grid size must increase as well [24].

2.2.2 Algorithm versions

The most basic FROG algorithm (the "Vanilla" algorithm) works by starting with an initial guess for the pulse $E(t)$, generating a signal field using the equation for $E_{sig}(t, \tau)$ based on the known FROG geometry, then iterating between the time and frequency domains, applying the measured FROG trace on each iteration, iteratively improving the guess until the measured trace and reconstructed trace are within a tolerance determined by the G error. This algorithm can, however, be prone to stagnation. A block diagram describing this algorithm is shown in Fig. 2.3 [24].

Until recently, existing algorithms showed reduced reliability as the pulse phase structure increased in complexity. A measure of pulse complexity is the TBP, defined as the product of the pulse's spectral and temporal FWHMs, and is dimensionless when frequency is measured in Hz [24]. For example, the vanilla iterative algorithm has a convergence rate of around 70% for pulses of TBPs $\approx$ 20 [29]. In our case, our linearly chirped pulses required for nonlinear microscopy have a TBP $\approx$ 10, high enough to be of concern for algorithm convergence.

To avoid algorithm stagnation and slow reconstruction, we used two more advanced FROG algorithm procedures. First, the Principal components generalized projections (PCGP) FROG algorithm is an implementation of a generalized projections algorithm, a robust algorithm frequently used in phase-retrieval applications. The technical details are discussed in great detail in the FROG textbook [24] and are beyond the scope of this thesis. In general, the PCGP FROG implementation resembles the Vanilla algorithm, but

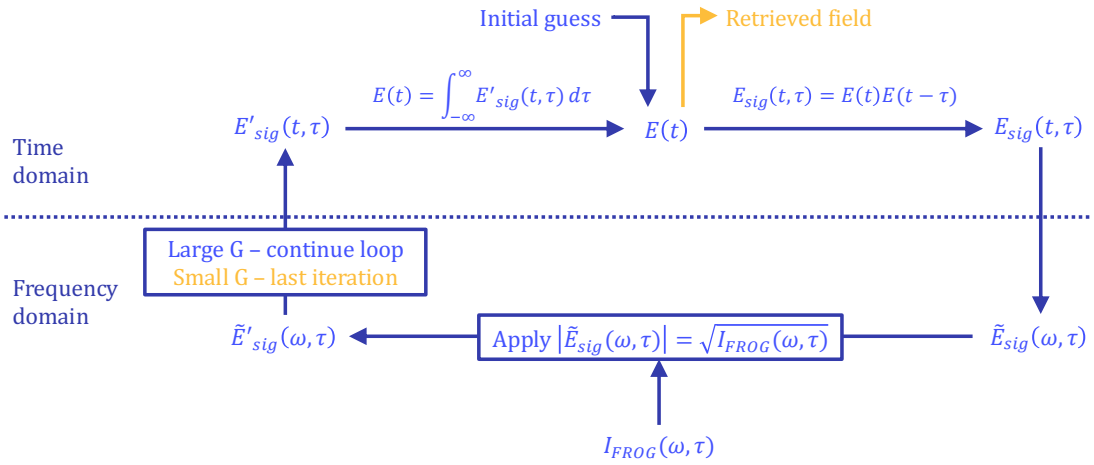

Figure 2.3: **Vanilla SHG FROG algorithm:** The basic algorithm starts by generating an initial guess for $E(t)$, which is then converted into a 2D FROG signal from the known mathematical form of the given geometry. The guess signal is then converted to the frequency domain so that it can be of the same form as the measured FROG trace. The magnitude of the guess FROG trace is then replaced by the square root of the measured trace, preserving the guess phase, generating the next guess for the FROG signal. This new generated signal is compared to the measured trace by the G error (Eq. (2.5)), if it is within the tolerance then this field will be returned, if not then the loop will continue to the next iteration. The FROG signal is converted back to the time domain, and a 1D field is generated by integrating over the delay, with the loop continuing until the chosen tolerance is met [24].

it performs a global principal-component (eigenvector) update of $E(t)$ upon each iteration that best fits all delays simultaneously, making it more robust to noise and less prone to stagnation.

A second improvement in FROG algorithms was developed in 2019 by the Trebino group, termed the Retrieved-Amplitude N-grid Algorithmic (RANA) FROG algorithm approach. RANA improves the initial guess for the pulse by directly retrieving the pulse spectrum amplitude from the measured trace, greatly reducing the number of iterations required for convergence. As well, early iterations use smaller grids ($N/4 \times N/4$ and

$N/2 \times N/2$) to increase speed, and guesses are routinely checked against the initial guess to verify that the algorithm is on a convergent path. Overall, RANA has a near 100% success rate on pulses substantially more complex than our pulses of TBP $\approx$ 10 with mostly linear chirp [29], and is available open-source [30], making it well suited to our needs.

There remains room to further increase algorithm speed and improve convergence for measurements with high noise or missing data. In 2025, three papers in *Optics Express* explored this topic, using iterative [31], ptychographic [32] and neural network [33] approaches. It may be worthwhile to investigate newer, more robust algorithms when looking to perform FROG reconstructions in the future.

3

Fringe-averaged collinear FROG

The following chapter is largely based on the 2024 paper by Frackleton et al [22], slightly restructured to improve flow, to add additional context and to discuss a broader range of uses than were covered in the original manuscript.

3.1 Motivation

In situ characterization of the electric field of ultrafast pulses is critical in multiphoton microscopy. While these signals can often be optimized using autocorrelation or cross-correlation measurements, some techniques benefit from the full pulse characterization at the sample plane of the microscope. Coherent control measurements, which rely on manipulating the spectral phase, fall under this category [10, 16, 17, 20, 21, 34]. In spectral focusing CRM, the achievable spectral resolution depends not only on the amount of chirp but also on whether the two input pulses are linearly chirped with matching slopes, as seen in Fig. 3.1. Higher-order chirps are harder to match and will generally result in poorer spectral resolution [17]. Performing FROG measurements to retrieve and correct the spectral phase of the input pump and Stokes pulses enables optimization of the chirp and, consequently, improved spectral resolution. Another similar use case is in CM-SRS microscopy (explored in detail in Part II), which uses two Stokes beams that are identical except for the sign of their linear chirp (quadratic phase). Here, in addition to the same spectral phase constraints on the pump and Stokes that apply to spectral focusing CRM, the relative spectral phase of the two Stokes beams influences the quality of background subtraction. To achieve optimal background subtraction, the two Stokes beams must have linear chirps of identical magnitude but opposite sign [10]. FROG therefore serves as a very useful tool for CM-SRS microscopy.

The collinear geometry required for laser scanning confocal microscopy makes conven-

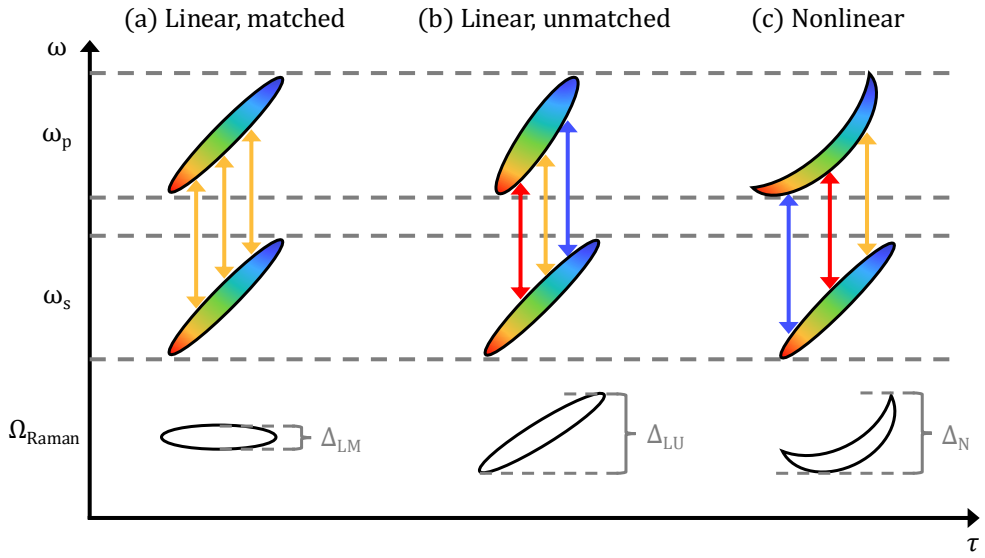

Figure 3.1: **Spectral resolution as a function of chirp:** The Raman resolution Δ_{Raman} at a given time point in the CRM spectral scan depends on the linearity and the matching of the two input chirps; ω_p, pump frequency; ω_s, Stokes frequency. (a): Ideal case, where both chirps have the same slope and are both linear, allowing for probing the narrowest possible bandwidth Δ_{LM} at a given time delay. (b): Two linear chirps but with different slopes; and (c): an input pulse with higher-order dispersion. Both non-ideal cases cause a larger bandwidth of Raman shifts (Δ_{LU} and Δ_N) to be probed per given time delay, leading to poorer spectral resolution [17].

tional noncollinear FROG methods unsuitable for *in situ* pulse characterization. Instead, a collinear FROG (cFROG) geometry will be necessary, but in this geometry, additional background and interference terms will be introduced [35, 36]. These new terms present three main challenges to the FROG method: 1) signal instabilities due to interferometric fringe drift; 2) high density sampling required to fully resolve the fringes, leading to longer acquisition times; and 3) the need to either remove the fringes from the acquired trace to allow the use of conventional FROG retrieval algorithms or to write new algorithms that leverage the interferometric data. Beyond the challenges associated with the collinear ge-

ometry, FROG characterization in microscopy settings can bring new complications. Many confocal microscopes make use of high Numerical aperture (NA) objectives that can cause distortions to the polarization state of the light at the focus, limiting the ability to use different polarization states of light to remove fringes. As well, FROG characterization of highly chirped pulses has unique challenges, including in reconstruction and long scan times, but is not as commonly addressed as the characterization of transform-limited and few-cycle pulses. Our goal is to develop a FROG modality that will address these issues and be ideal for use in nonlinear microscopy implementations.

3.2 Introduction

FROG, with its many advantages in laser pulse characterization, has been adapted to collinear geometries for a variety of purposes, including use at the sample plane in nonlinear microscopy and for its robustness to geometrical smearing compared to conventional non-collinear FROG methods [35–37]. However, each adaptation introduces specific technical challenges or limitations. The first implementation of cFROG was based on orthogonally polarized input pulses from the interferometer, combined with type II phase matching [37–39], demonstrating the characterization of sub-20 fs pulses at the focus of a high NA objective. Technical challenges associated with this approach can include impure polarization states at the focal plane, leading to residual fringes, and the asymmetric deformation of the FROG traces due to the temporal walk-off of the orthogonal polarizations [38]. Impure polarization states can particularly arise in commercial microscope systems where

there is limited access and control over residual birefringence, and in high-NA objectives where polarization aberrations are common [40, 41]. To address this, type I-based cFROG with low-pass Fourier filtering of the interferometric contributions was implemented [35]. However, a fully sampled type I cFROG scan requires a small delay step size to satisfy Nyquist sampling requirements, leading to long scan times for chirped pulses. This can be mitigated by careful undersampling of the type I cFROG scan, provided that some a priori knowledge of the pulse profiles exists [35]. This approach works for simple pulses but aliasing becomes an issue for complex pulse shapes.

Although simple and attractive, cFROG augmented by Fourier filtering alone does not fully address interferometric drift. If there is any drift or noise in the interferometric term (delay line jitter, temperature-induced pointing change, etc.) over the course of data acquisition, this results in the interference term having low-frequency components that cannot be removed by Fourier filtering. A proposed solution was to increase the acquisition speed using a continuously scanned delay stage rather than step-scan data acquisition [36]. Here, a new FROG algorithm was developed to extract the electric field directly from the interferometric term, with no Fourier filtering of the fringes. This approach is indeed robust with respect to drift but requires a specialized retrieval algorithm and relatively dense data sets leading to longer acquisition times. In addition to SHG cFROG, THG-based FROG was also demonstrated in the collinear geometry [42, 43]. However, its lower (than SHG) sensitivity for chirped pulses and ultraviolet signal generation necessitating dedicated collection optics make THG-cFROG less practical for most multiphoton microscopy settings.

In an alternative approach to cFROG, a spatial light modulator-based 4f-pulse shaper

was used to produce phase-locked pulse pairs to perform FROG scans. This alleviated the need for conventional Michelson or Mach-Zehnder interferometers and further allowed to use the relative carrier-envelope phase (CEP) as a degree of freedom to increase the period of the fringes to reduce the density of sampling points in cFROG [44]. However, care must be taken with spatial light modulators so as to avoid diffractive effects (space-time coupling) that may significantly complicate the analysis of tightly focused beams [45]. An acousto-optic programmable dispersive filter (e.g., Dazzler) can also create pulse pairs and manipulate the relative CEP [46]. This variant, baseband FROG (bFROG), extracts the upper envelope of the interferometric FROG trace, solving the sampling problem but requiring a new field retrieval algorithm. Alternatively, a phase-cycled FROG approach was developed through cancelling the fringes by summing contributions from four different relative CEP values [47]. A concern here is that the finite interaction length within acousto-optic crystals may limit the ability of these techniques to simultaneously chirp the pulses and scan long delays. Finally, although these strategies do provide phase-locked pulse pairs, they also require instrumentation more advanced than typically found in standard laser scanning microscopy labs.

Here we present a simple and effective cFROG modality, FRACOL-FROG, which is well suited to *in situ* pulse characterization of highly chirped pulses. FRACOL-FROG is based on actively dithering the interferometric path length difference to smooth out the interference term present in typical cFROG setups. By implementing a kHz-driven piezo retroreflector in the non-scanning arm of a Mach-Zehnder interferometer, we average over optical fringes at each step of the delay scan stage, thus making the measurement

insensitive to interferometric drifts. In addition, the implicit robustness to aliasing allows the undersampling of the cFROG trace, thereby significantly reducing the sampling density. Finally, the removal of fringes enables use of the conventional SHG FROG algorithm. In the following, we present our analytical model of FRACOL-FROG and demonstrate its successful experimental implementation.

3.3 Model

We derive an analytical expression for the FRACOL-FROG signal, following closely the analysis presented in [36]. We start with a laser pulse $\mathcal{E}(t) = \mathcal{R}e\{\underline{\mathrm{E}}(t)\}$, with $\underline{\mathrm{E}}(t)$ an analytic function. In the slow-varying envelope approximation, $\underline{\mathrm{E}}(t)$ can be written as the product of a slowly varying complex amplitude $E(t)$ and a fast-oscillating term at the carrier angular frequency ω_0:

$$\underline{\mathrm{E}}(t) = E(t)\exp(i\omega_0 t). \tag{3.1}$$

Noncollinear SHG FROG spectrally resolves the autocorrelation of this electric field:

$$I_{FROG}(\omega,\tau) \propto \left|\int_{-\infty}^{\infty} \underline{\mathrm{E}}(t)\underline{\mathrm{E}}(t-\tau)\exp(-i\omega t)\mathrm{d}t\right|^2. \tag{3.2}$$

In cFROG, the recorded signal becomes:

$$I_{cFROG}(\omega,\tau) \propto \left|\int_{-\infty}^{\infty} [\underline{\mathrm{E}}(t)+\underline{\mathrm{E}}(t-\tau)]^2\exp(-i\omega t)\mathrm{d}t\right|^2, \tag{3.3}$$

where τ is the relative delay between the two interferometer arms.

In FRACOL-FROG, signal acquisition involves active dithering of the interferometer path length difference using a piezo-driven retroreflector (shaker). The shaker must average over optical fringes during the spectrometer integration time T_{int} in order to effectively remove them. The resultant signal is:

$$I_{FRACOL-FROG}(\omega,\tau) \propto \int_{-N\Delta T/2}^{N\Delta T/2} \underbrace{\underbrace{\left| \underbrace{\int_{-\infty}^{\infty} \underbrace{[\underline{\mathrm{E}}(t-t') + \underline{\mathrm{E}}(t-\tau)]^2}_{A_1} \exp(-i\omega t)\mathrm{d}t}_{A_2=FT\{A_1\}} \right|^2}_{A_3=A_2\cdot A_2^*} \mathrm{d}t'}, \quad (3.4)$$

where the second integral over t' averages (sums) over the periodic motion of the shaker. The amplitude of the shaker displacement independently sets the number of optical wavelengths the path length difference traverses during one shaker period. We express this here in the time domain as ΔT, related to the number of optical periods traversed during one cycle of the shaker. The shaker period is T_{sh} and, to effectively remove fringes, it must be a small fraction of the spectrometer integration time T_{int}. The ratio $N = T_{int}/T_{sh}$ indicates how many shaker periods exist within T_{int}. For example, in our implementation, the spectrometer integration time was set to $T_{int} = 20$ ms, and the shaker was driven at 2 kHz ($T_{sh} = 0.5$ ms), resulting in N = 40. To evaluate the integral in Eq. (3.4), we consider

it in three steps A_1, A_2 and A_3. We expand A_1 using Eq. 3.1:

$$\begin{aligned} A_1(t,t',\tau) &= [\underline{\mathrm{E}}(t-t') + \underline{\mathrm{E}}(t-\tau)]^2 \\ &= E^2(t-t')\exp(2i\omega_0(t-t')) + E^2(t-\tau)\exp(2i\omega_0(t-\tau)) \\ &\quad + 2E(t-t')E(t-\tau)\exp(i\omega_0(t-t'))\exp(i\omega_0(t-\tau)). \end{aligned} \tag{3.5}$$

A_2 is the Fourier transform FT of the above expansion of A_1:

$$\begin{aligned} A_2(\omega,t',\tau) &= \int_{-\infty}^{\infty} A_1(t,t',\tau)\exp(-i\omega t)\mathrm{d}t \\ &= \int_{-\infty}^{\infty} E^2(t-t')\exp(2i\omega_0(t-t'))\exp(-i\omega t)\mathrm{d}t \\ &\quad + \int_{-\infty}^{\infty} E^2(t-\tau)\exp(2i\omega_0(t-\tau))\exp(-i\omega t)\mathrm{d}t \\ &\quad + \int_{-\infty}^{\infty} 2E(t-t')E(t-\tau)\exp(i\omega_0(t-t'))\exp(i\omega_0(t-\tau))\exp(-i\omega t)\mathrm{d}t. \end{aligned} \tag{3.6}$$

Following the treatment in [36], with $\Delta\omega = \omega - 2\omega_0$, we define the second harmonic field of a single pulse (E_{SHG}) and the FROG field (E_{FROG}) as:

$$E_{SHG}(\Delta\omega) = \int_{-\infty}^{\infty} E^2(t'')\exp(-i\Delta\omega t'')\mathrm{d}t'', \qquad t'' = t - t' \tag{3.7}$$

$$E_{FROG}(\Delta\omega,t',\tau) = \int_{-\infty}^{\infty} E(t'')E(t''+t'-\tau)\exp(-i\Delta\omega t'')\mathrm{d}t''. \tag{3.8}$$

This allows the recasting of Eq. 3.6 as:

$$\begin{aligned} A_2(\omega, t', \tau) = &\exp(-i(2\omega_0 + \Delta\omega)t')E_{SHG}(\Delta\omega) + \exp(-i(2\omega_0 + \Delta\omega)\tau)E_{SHG}(\Delta\omega) \\ &+ 2\exp(-i(\omega_0 + \Delta\omega)t')\exp(-i\omega_0\tau)E_{FROG}(\Delta\omega, t', \tau). \end{aligned} \tag{3.9}$$

A_3 can therefore be written as:

$$\begin{aligned} A_3(\omega, t', \tau) &= A_2(\Delta\omega, t', \tau) \cdot A_2^*(\Delta\omega, t', \tau) \\ &= 2|E_{SHG}(\Delta\omega)|^2 + 4|E_{FROG}(\Delta\omega, t', \tau)|^2 \\ &\quad + 2|E_{SHG}(\Delta\omega)|^2 \cos[(2\omega_0 + \Delta\omega)(t' - \tau)] \\ &\quad + 8\cos\left[\left(\omega_0 + \frac{\Delta\omega}{2}\right)(t' - \tau)\right] \mathcal{R}e\{E_{FROG}(\Delta\omega, t', \tau) \\ &\qquad\qquad E_{SHG}^*(\Delta\omega)\exp\left[\frac{i\Delta\omega}{2}(t' - \tau)\right]\}. \end{aligned} \tag{3.10}$$

In the absence of the shaker (i.e., removing t'), the above expression for the signal reduces, as expected, to that of conventional SHG cFROG [36]:

$$\begin{aligned} I_{cFROG}(\omega, \tau) &\propto A_3(\omega, \tau) \\ &\propto 2|E_{SHG}(\Delta\omega)|^2 + 4|E_{FROG}(\Delta\omega, \tau)|^2 \\ &\quad + 2|E_{SHG}(\Delta\omega)|^2 \cos[(2\omega_0 + \Delta\omega)\tau] \\ &\quad + 8\cos\left[\left(\omega_0 + \frac{\Delta\omega}{2}\right)\tau\right] \mathcal{R}e\left\{E_{FROG}(\Delta\omega, \tau)E_{SHG}^*(\Delta\omega)\exp\left(\frac{i\Delta\omega}{2}\tau\right)\right\}. \end{aligned} \tag{3.11}$$

In both cases, the first term is the delay-independent second harmonic background, which

can be subtracted by measuring the signal at longer delays. The second term is the noncollinear FROG signal. The third and the fourth terms are the interferometric terms contributing to the sidebands at $\pm 2\omega_0$ and $\pm\omega_0$, respectively. A quantity of interest here is the delay marginal M(τ), defined as [28]:

$$M(\tau) = \int I_{cFROG}(\omega, \tau)\mathrm{d}\omega, \tag{3.12}$$

which in this case is the interferometric autocorrelation trace. The peak-to-background ratio of this trace should be 8:1, with the SHG intensity at maximal overlap coming from the coherent addition of two fields, and the SHG intensity at long delays coming from the incoherent addition of two fields [48, 49]. This ratio can be used to confirm the integrity of the FROG interferometer. This is depicted in Fig. 3.2(a) for a Gaussian envelope light field $\mathcal{E}(t) = \exp(-t/2\sigma^2)\cos(\omega_0 t)$, where ω_0 is the central angular frequency and σ is related to the FWHM of the laser pulse. A cFROG measurement with this light field yields the black delay marginal in Fig. 3.2(b) with the characteristic peak-to-background ratio.

We now introduce the shaker, modifying the I_{cFROG} signal. Substituting Eq. (3.10) in Eq. (3.4):

$$I_{FRACOL-FROG}(\omega, \tau) \propto \int_{-N\Delta T/2}^{N\Delta T/2} A_3(\omega, t', \tau)\mathrm{d}t'. \tag{3.13}$$

For FRACOL-FROG to average out the sidebands at $\pm\omega_0$ and $\pm 2\omega_0$ while not perturbing the noncollinear FROG spectrogram due to path length dithering, two conditions

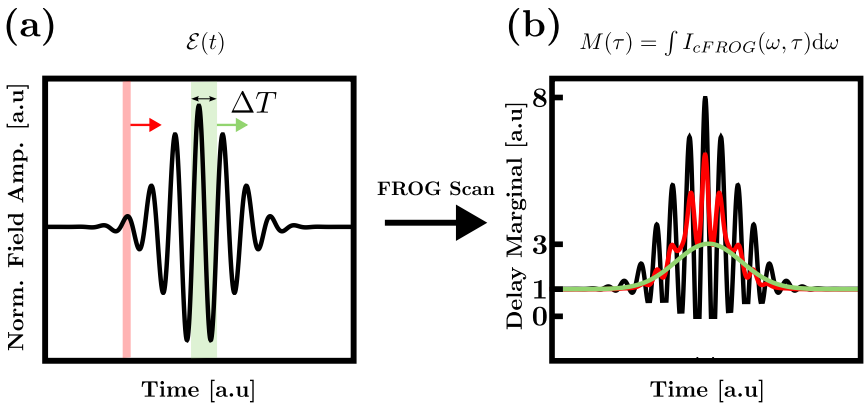

Figure 3.2: **Principle of FRACOL-FROG**: (a): We show the field of the laser pulse, assuming a Gaussian envelope: $\mathcal{E}(t) = \exp(-t/2\sigma^2)\cos(\omega_0 t)$. The green- and red-shaded windows depict two characteristic cases for the shaker temporal amplitude ΔT. For the red window, $\Delta T < 2\pi/\omega_0$, whereas for the green window, $\Delta T = 2\pi/\omega_0$. (b): Delay marginals of cFROG measurements with path length dithering of $\Delta T = 0$ (black), $\Delta T < 2\pi/\omega_0$ (red), and $\Delta T = 2\pi/\omega_0$ (green). In the case of $\Delta T = 2\pi/\omega_0$, the fringes integrate to zero, yielding a conventional noncollinear SHG FROG trace.

must be met:

1. The time domain displacement (amplitude) of the shaker, ΔT, must be less than the shortest temporal feature in the pulse. For a well-behaved pulse, this translates to $\Delta T \ll \Delta\tau_{FWHM}$, where $\Delta\tau_{FWHM}$ is the FWHM of the pulse intensity envelope. In this case, the magnitude of the field envelope can be considered constant over the shaker displacement range, i.e., $E_{FROG}(\Delta\omega, t', \tau) \approx E_{FROG}(\Delta\omega, \tau)$. Given that the maximum displacement of the shaker is typically hundreds of nanometres, equivalent to a time delay of a few femtoseconds, this is a valid assumption for pulses of transform-limited temporal FWHM on the order of 100 fs. This constraint is further relaxed for linearly chirped pulses (FWHM ∼1 ps), commonly used in spectral

focusing CRM, where the pulse FWHM will be orders of magnitude larger than the time domain displacement of the shaker.

2. The time domain amplitude of the shaker, ΔT, must be chosen such that $\mathrm{mod}_{\frac{2\pi}{\omega_0}}[\Delta T] = 0$. By integrating t' over one (or an integer multiple) period $2\pi/\omega_0$ of the carrier wave, the oscillating terms in Eq. (3.13) at $\pm\omega_0$ (fourth term) and $\pm 2\omega_0$ (third term) will integrate to zero. This is depicted by the green window case of Fig. 3.2(a) and green curve in Fig. 3.2(b) . Cases when this condition is not met lead to residual fringes (red window of Fig. 3.2(a) and red curve in Fig. 3.2(b)). For example, with a central wavelength of 800 nm, this sets $\Delta T = n$ 2.7 fs (where $n \in \mathbb{N}$) for complete fringe removal. Under experimental conditions, this is a very strict requirement and is hard to be met. However, it is enough to be close to the condition for leveraging the benefits of FRACOL-FROG. This is further elaborated in Section 3.4 - Methods, Fig. 3.4.

When both conditions are met, the expression for $I_{FRACOL-FROG}(\omega, \tau)$ simplifies to:

$$I_{FRACOL-FROG}(\omega, \tau) \propto 2|E_{SHG}(\Delta\omega)|^2 N\Delta T + 4|E_{FROG}(\Delta\omega, \tau)|^2 N\Delta T. \tag{3.14}$$

Upon subtraction of the delay-independent term, the conventional noncollinear SHG FROG signal can be extracted and processed using standard algorithms.

3.4 Methods

The FRACOL-FROG system, depicted in Fig. 3.3, comprises a dispersion-balanced Mach-Zehnder interferometer built on a 12'x12' breadboard with a motorized scanning delay stage (MFA-CC, Newport) on the variable delay arm and a piezo-driven shaker on the fixed arm. The shaker was toggled on for FRACOL-FROG measurements and toggled off for cFROG measurements. The power of the tunable output (960 nm) of a dual output femtosecond laser system (Insight X3, Spectra-Physics) was attenuated using a half-wave plate (HWP)-polarizing beam splitter (PBS) combination before coupling into the FRACOL-FROG setup. Using matched beam splitters (UFBS5050, Thorlabs), the input beam was split and recombined collinearly. The output was subsequently routed using a flip mirror to either perform tabletop measurements or *in situ* measurements at the microscope focal plane.

For the tabletop measurements, as seen in Fig. 3.3(a), the collinear overlapped beams were focused onto a type I Beta Barium Borate (β-BBO) crystal ($\theta = 31°$) of 2 mm thickness. The SHG signal was isolated from the fundamental beam using a shortpass filter (FF01-488/50-25, Semrock) and coupled into a spectrometer (HR4Pro, Ocean Optics) using an integrating sphere so as to remove spatial effects while coupling into the fibre spectrometer. We performed cFROG (shaker off) and FRACOL-FROG (shaker on) measurements with differing amounts of known linear dispersion, ranging from zero added dispersion (the transform-limited pulse, $\sim$130 fs) to a highly dispersed pulse ($\sim$1.5 ps).

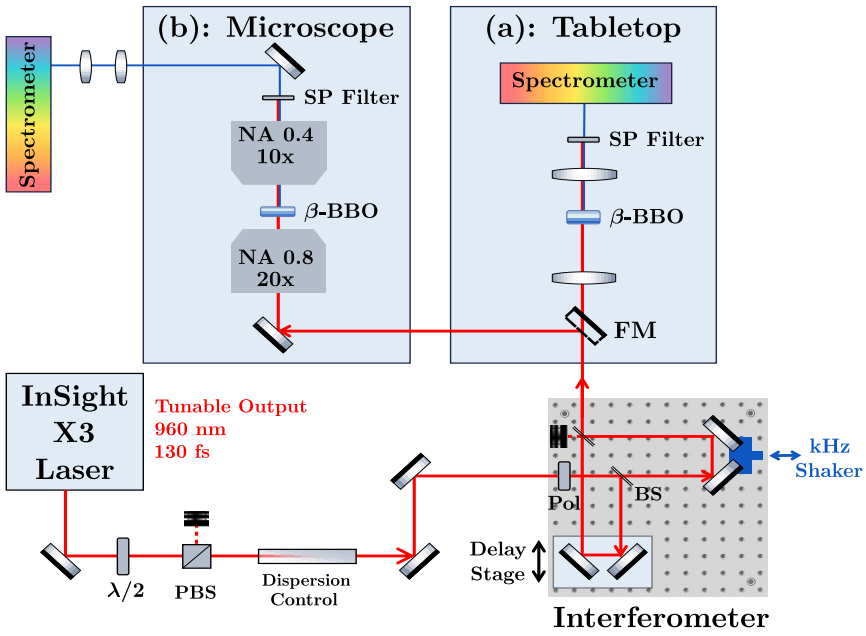

Figure 3.3: **Experimental implementation of FRACOL-FROG:** The demonstration of FRACOL-FROG was achieved via both (a) proof-of-concept tabletop measurements and (b) measurements made at the focal plane of a high NA microscope objective. Abbreviations for the optical elements shown are: $\lambda/2$, half-wave plate; PBS, polarizing beam splitter; BS, 50/50 beam splitter; Pol, Polarization control; FM, flip mirror; β-BBO, Beta Barium Borate type I crystal; SP filter, shortpass filter.

The added dispersive elements used were one or two 10 cm-long N-SF11 rods (SF11L1100-AR800, Newlight) or one 10 cm-long rod of non-crystalline ZnSe. To confirm the accuracy of the FRACOL-FROG measurements and their reconstruction, the retrieved spectral phases of the chirped pulses were compared to the expected theoretical results obtained using the known Sellmeier equations for N-SF11 [50] and ZnSe [51] materials.

To demonstrate *in situ* microscopy measurements, the output of the FRACOL-FROG system was directed to a custom multimodal nonlinear microscope (FV3000 Confocal Mi-

croscope, Evident), the confocal geometry of which is shown in Fig. 3.3(b). The type I SHG crystal used in these measurements was a 0.2 mm β-BBO crystal (BTC5020-SHG1030(I)-P, Newlight) placed at the sample plane of the microscope. The incoming light was focused using a 20x 0.8 NA objective (UPLXAPO20X, Evident) and collected using a 10x 0.4 NA objective (UPLXAPO10X, Evident). A shortpass filter (FF01-488/50-25, Semrock) transmitted the SHG signal. Upon the output beam size being reduced using a 3:1 telescope, the SHG signal was coupled to the spectrometer. Note that for measurements in the microscope, a fixed amount of dispersion was used, consisting of a double pass through five 10 cm-long N-SF11 rods.

A delay step size of 0.5 fs was used in order to fully resolve the sideband at $2\omega_0$ of 1.6 fs period. The integration time of the spectrometer for all the measurements was set to 20 ms. The delay scan ranges were chosen based on the amount of dispersion, so as to measure the tails of the FROG spectrogram. In order to subtract the delay-independent SHG background term in Eq. (3.14), a background measurement was done, following each FROG scan, by moving the delay stage far from time zero.

The piezo element of the shaker was from a generic 75W 2-1/8" x 5-3/4" horn tweeter. The centre of the element was cemented to the thread end of an 8/32 screw. The head of the screw was cemented centrally to the retroreflector assembly. A 1/4" thin optical post was used to mount the retroreflector to enhance the amplitude of the shaking. For the FRACOL-FROG measurements, the shaker was driven at 2 kHz using a ramp waveform from an arbitrary waveform generator (RIGOL model DG822), with the driving voltage, which controls the shaker amplitude, tuned to maximize fringe suppression. While it

would be ideal to use a shaker amplitude that satisfies the condition for perfect fringe suppression as described above in Section 3.3 - Model, this is hard to achieve under practical experimental conditions. However, to benefit from the robustness offered by FRACOL-FROG, it is enough to find the shaker displacement that corresponds to near-ideal (but not total) fringe suppression, and the residual fringes can be removed via Fourier filtering. To highlight this, we performed FRACOL-FROG measurements of pulses stretched using 10 cm of N-SF11 glass, with ΔT values corresponding to 1) minimal fringe suppression, 2) some fringe suppression, and 3) near-ideal fringe suppression, as seen in Fig. 3.4. As the shaker amplitude is tuned to match the carrier wave period, the fringes are better averaged out (Fig. 3.4, top and middle rows). At the same time, the frequency terms close to the DC band are greatly suppressed (Fig. 3.4, bottom row), allowing us to define an unambiguous width for the Fourier filter to isolate the DC band.

Following the methods of prior cFROG-based techniques, the base-level background was subtracted from the trace, and any residual fringes were removed via Fourier low-pass filtering along the delay axis using a fourth-order super-Gaussian window function [52]. The FROG reconstruction was achieved through the RANA PCGP algorithm MATLAB implementation by the Trebino group [30].

3.5 Results and Discussion

Both cFROG and FRACOL-FROG measurements follow the same protocols, with the simple addition of the shaker for FRACOL-FROG. A comparison of cFROG and FRACOL-

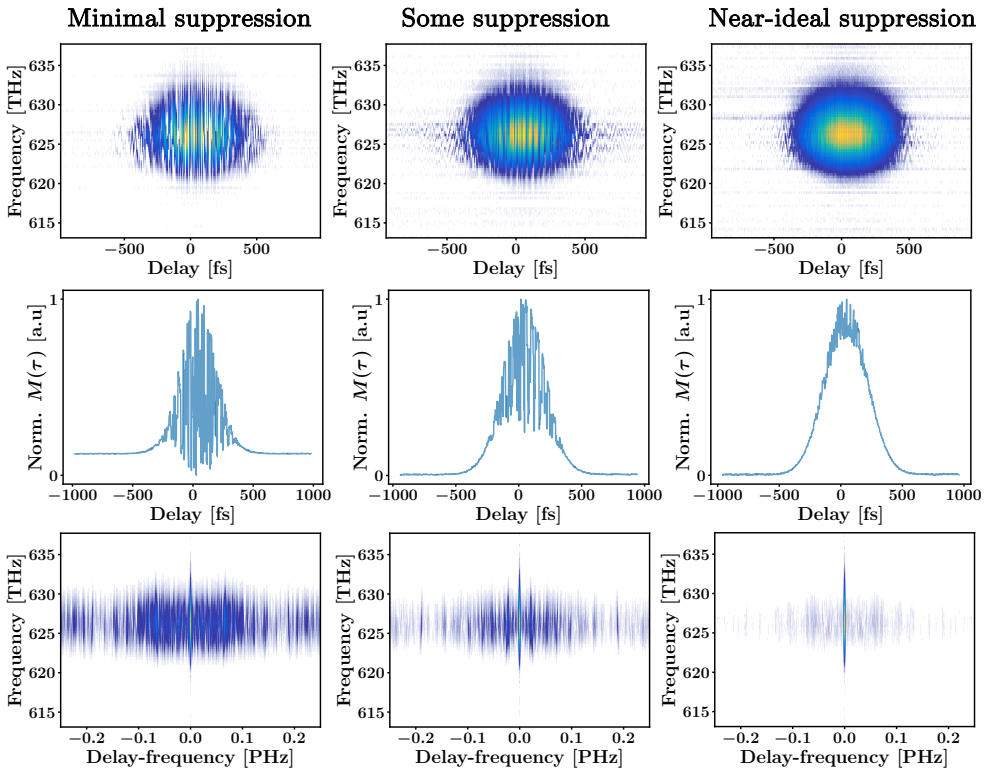

Figure 3.4: **Fringe suppression as a function of shaker temporal amplitude:** We compare three cases of the shaker temporal amplitude for FRACOL-FROG measurements of a pulse propagating through 10 cm of N-SF11 glass. (a)-(c): Measured FROG traces. (d)-(f): Delay marginals $M(\tau)$. (g)-(i): Fourier transform with respect to the delay axis of the measured FROG traces. In each row, we see that the right column, corresponding to near-ideal fringe suppression, is close to a conventional non-collinear SHG FROG trace, whereas the left column, corresponding to minimal suppression, is close to a cFROG trace. The middle column shows some fringe suppression, but with room for improvement.

FROG measurements of a transform-limited pulse is shown in Fig. 3.5. The delay marginal

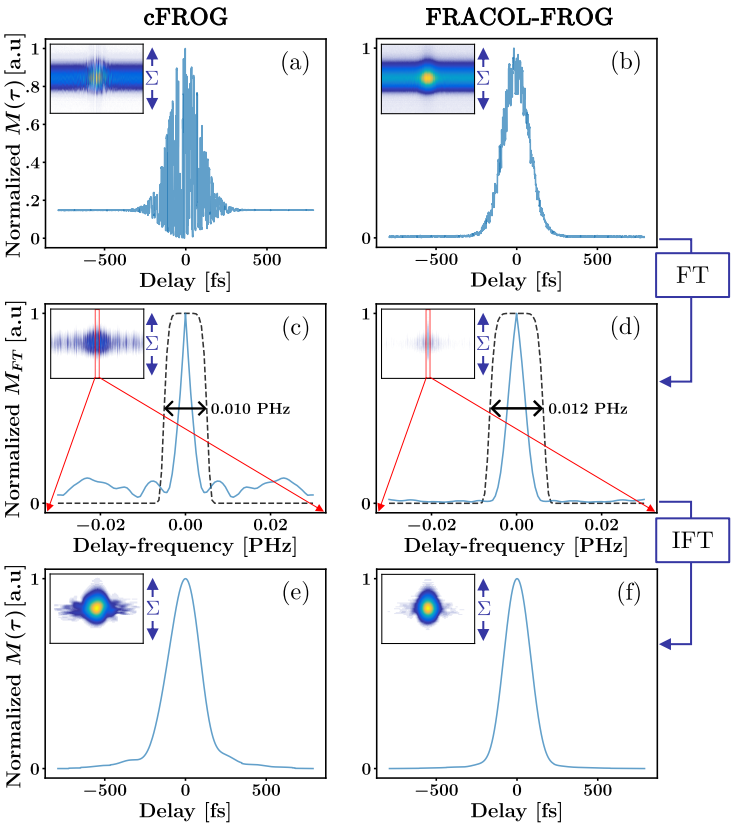

Figure 3.5: **Marginal comparison of cFROG with FRACOL-FROG:** cFROG (left column) and FRACOL-FROG (right column) measurements of a transform-limited pulse. Σ: axis of summation for the marginal computation. (a), (b): Delay marginals $M(\tau)$ of the measured FROG traces (insets). The peak-to-background ratio in (a) is ≈6.5:1. (c), (d): Marginals M_{FT} of the Fourier transforms (FT) with respect to the delay axis (insets) of background-subtracted traces in insets of a) and b). Only the region of the marginal around the DC band is shown (red bands on inset). It can be seen that the cFROG result is much noisier. The central peak is next multiplied with a fourth-order super-Gaussian window function (dashed black line) with width chosen by the analysis presented in Fig. 3.7 (vide infra), providing a Fourier domain removal of the high frequency terms. (e), (f): Delay marginals $M(\tau)$ of the Fourier filtered measured FROG traces (insets). The FRACOL-FROG measurement is seen to have an improved delay marginal profile. See Fig. 3.6 for the reconstruction results corresponding to this FRACOL-FROG measurement.

for the cFROG spectrogram (inset), seen in Fig. 3.5(a), is equivalent to an interferometric autocorrelation trace. Here, the peak-to-background is approximately 6.5:1, attributed to imperfect beam splitting in the FROG device, to lack of precision in the optical alignment and to interferometric instabilities. After subtraction of the constant background term, the spectrogram undergoes a Fourier transform along the delay axis to allow for low-pass filtering. Fig. 3.5(c) shows the marginal of this Fourier transform (inset), with significant noise near the DC band, attributed to the step-scan motion of the delay stage [53] and to interferometric drift effects. The transformed 2D spectrogram (inset) is multiplied with a fourth-order super-Gaussian window, the width of which is chosen by analysis as described in Fig. 3.7. Applying an inverse Fourier transform, we obtain a FROG spectrogram equivalent to a non-collinear SHG FROG trace, with the delay marginal as shown in Fig. 3.5(e). Figs. 3.5(b), 3.5(d), 3.5(f) present the analogous plots from the FRACOL-FROG measurement. As anticipated, it is seen from Fig. 3.5(b) that the delay marginal of the FRACOL-FROG trace looks similar to a non-collinear autocorrelation. We note that the presence of residual fringes is due to the shaker displacement not exactly matching the optical period of the carrier wave, and not due to impure states of polarization as in the case of type II cFROG [37]. In future implementations, this could be improved with a finer control piezo element. Despite the residual fringes, it is seen from Fig. 3.5(d) that the shaker averaging effectively cancels the noise around the DC band, allowing for Fourier filtering with confidence and obtaining a more Gaussian-like delay marginal, as shown in Fig. 3.5(f).

The Fourier filtered FRACOL-FROG spectrogram of Fig. 3.5(f) was passed to the

FROG algorithm, the results of this electric field retrieval are shown in Fig. 3.6. The

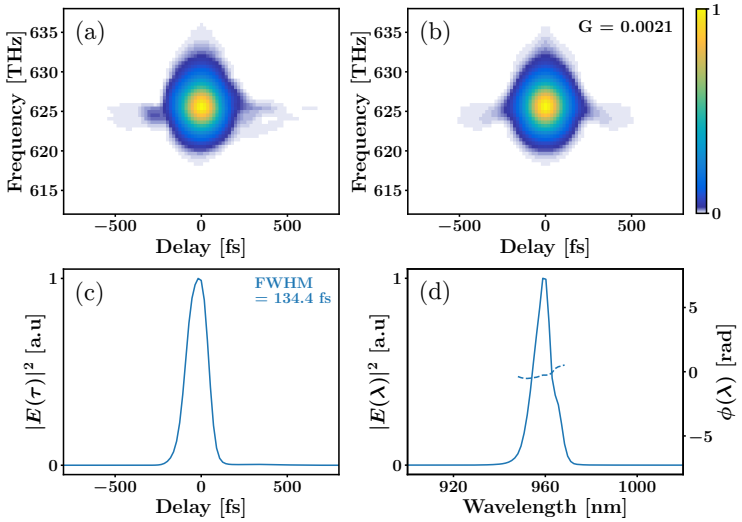

Figure 3.6: **Reconstruction results for the transform-limited pulse in Fig. 3.5:** We pass the Fourier filtered FRACOL-FROG data from Fig. 3.5(f) to the field retrieval algorithm. (a) Filtered measured trace, binned to a 128×128 grid. (b) Reconstructed trace with FROG G error 0.0021. (c) Retrieved temporal intensity, pulse duration showing good agreement with the laser specifications. (d) Retrieved spectral intensity (solid line) and phase (dashed line). We get a near-flat spectral phase, as expected for a transform-limited pulse.

FROG G error was found to be 0.0021 for a 128×128 grid, indicating successful convergence [24].

For cFROG measurements, the noise around the DC band imposes constraints on the optimal filter window bandwidth, making data processing more challenging. This effect is shown in Fig. 3.7. The super-Gaussian window has a range of bandwidths constrained by the dual requirements of fully encompassing the DC band and eliminating the non-DC noise terms. Applying a range of filter bandwidths, shown in Fig. 3.7(a), leads to considerable variation in the filtered delay marginals, shown in Fig. 3.7(c). A filter that is too narrow

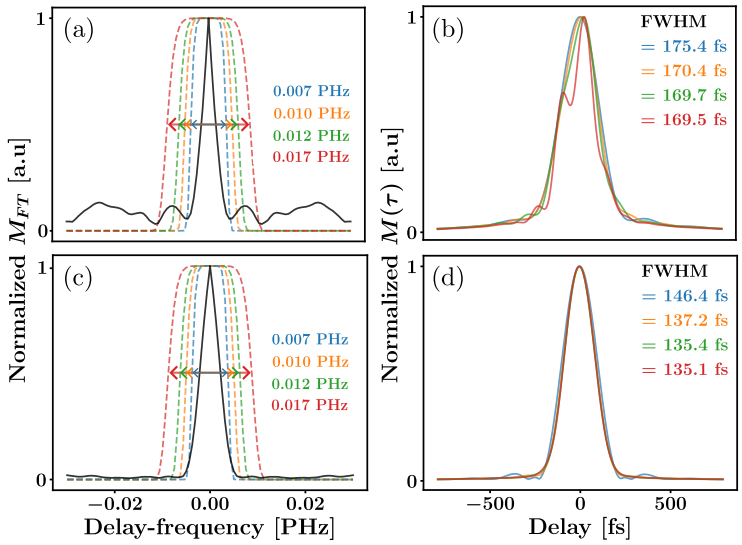

Figure 3.7: **Fourier filtering of cFROG and FRACOL-FROG:** We compare the effect of the width of the super-Gaussian function for Fourier filtering on cFROG (top row) and FRACOL-FROG (bottom row). (a), (c): The black curves are the delay axis Fourier transform marginals of the measured FROG traces from Fig. 3.5. The coloured curves show the broad range of super-Gaussian window widths used for Fourier filtering. (b), (d): Corresponding Fourier filtered FROG delay marginals as a function of the super-Gaussian bandwidth. The FWHM values of the delay marginals are given for comparison. It can be seen in (d) that FRACOL-FROG exhibits less variance with respect to the choice of super-Gaussian width.

may partially remove the DC band, increasing susceptibility to Fourier transform aliasing and leading to signal broadening. A filter that is too wide does not effectively remove the fringes. In contrast, applying the same range of filter bandwidths to the FRACOL-FROG results, shown in Fig. 3.7(b), shows good stability in the filtered delay marginals for windows that fully retain the DC band, as seen in Fig. 3.7(d). Thus, fringe averaging reduces the noise around the DC band, which, in turn, relaxes the constraints on the super-Gaussian filter bandwidth.

The reproducibility of the FROG scans is another important consideration. In Fig. 3.8, we show the reproducibility of the Fourier filtered delay marginals for three repeated sequential scans. In Fig. 3.8(a), we show this sensitivity for the cFROG scans and, in Fig.

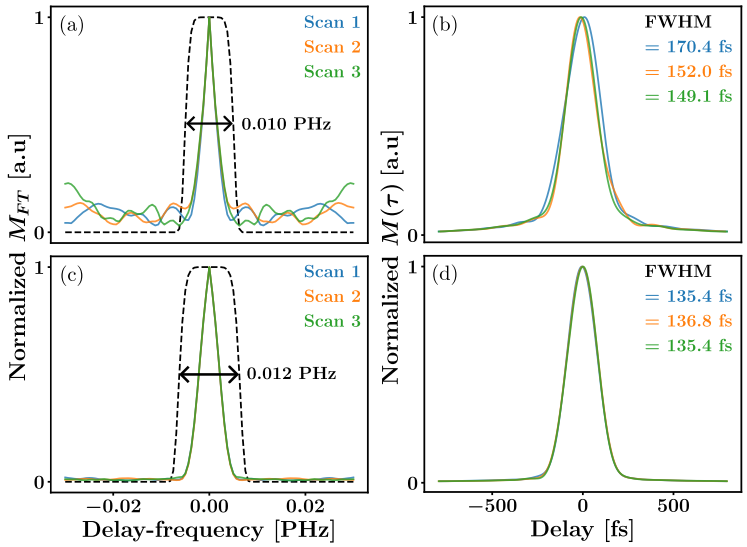

Figure 3.8: **Experimental reproducibility of cFROG versus FRACOL-FROG:** We compare the reproducibility of cFROG (top row) and FRACOL-FROG (bottom row) across three sequential scans. (a), (c): Delay axis Fourier transform marginals (coloured traces) of measured FROG traces for three sequential scans. The width of super-Gaussian windows (black dashed lines) used for Fourier filtering were determined from Fig. 3.7. (b), (d): Corresponding filtered delay marginals of the three sequentially repeated FROG traces. The FWHM values of the delay marginals are given for comparison. The much narrower spread in FWHM values for the FRACOL-FROG (standard deviation of 0.7 vs 10) indicates its superior stability and reproducibility.

3.8(c), for the FRACOL-FROG scans. The corresponding Fourier filtered delay marginals are shown in Figs. 3.8(b) and 3.8(d), respectively. Comparing the FWHMs of the Gaussian fits of the filtered delay marginals for both modalities, it is seen that scan reproducibility is much improved by FRACOL-FROG. Of note, in Figs. 3.7 and 3.8, the FWHM is larger

for the cFROG scans due to the presence of noise around the DC term. This results in a broader pulse in time in comparison to an analogous FRACOL-FROG measurement.

Next, we confirm the accuracy of the FRACOL-FROG method by characterizing pulses with carefully controlled, variable degrees of dispersion, as shown in Fig. 3.9. To achieve this, we propagated the transform limited pulses through 10 cm of N-SF11 glass, 20 cm of N-SF11 glass, and 10 cm of non-crystalline ZnSe. The known Sellmeier coefficients of these standard optical materials permit direct calculation of the expected pulse dispersion. The FRACOL-FROG measurements at three different dispersions are shown in Figs. 3.9(a)-3.9(c). In Figs. 3.9(d)-3.9(f), we show the filtered traces binned to a 256×256 grid for both N-SF11 scans, and to a 512×512 for the ZnSe scan. In Figs. 3.9(g)-3.9(i), we show the reconstructed traces for each case, with FROG G error values of 0.0015, 0.0027 and 0.0025, respectively. In Figs. 3.9(j)-3.9(l), we plot the retrieved spectral intensity and second-order phase for each case. We compare these with the values computed from the Sellmeier coefficients for these materials; it can be seen that the retrieved and calculated second-order phases agree very well. In Figs. 3.9(m)-3.9(o), we plot the retrieved temporal intensity and their FWHM for each of the three dispersion cases. This study confirms the accuracy of the FRACOL-FROG method in determining the electric fields of strongly chirped pulses.

Finally, we demonstrate *in situ* measurements using FRACOL-FROG in a nonlinear microscope setup as described in Fig. 3.3(b). We successfully characterize, *in situ*, a strongly chirped laser pulse, as seen in Figs. 3.10(a)-3.10(d), obtaining a FROG G error of 0.0043 on a 1024×1024 binned grid. It is seen that, accounting for all the dispersion in

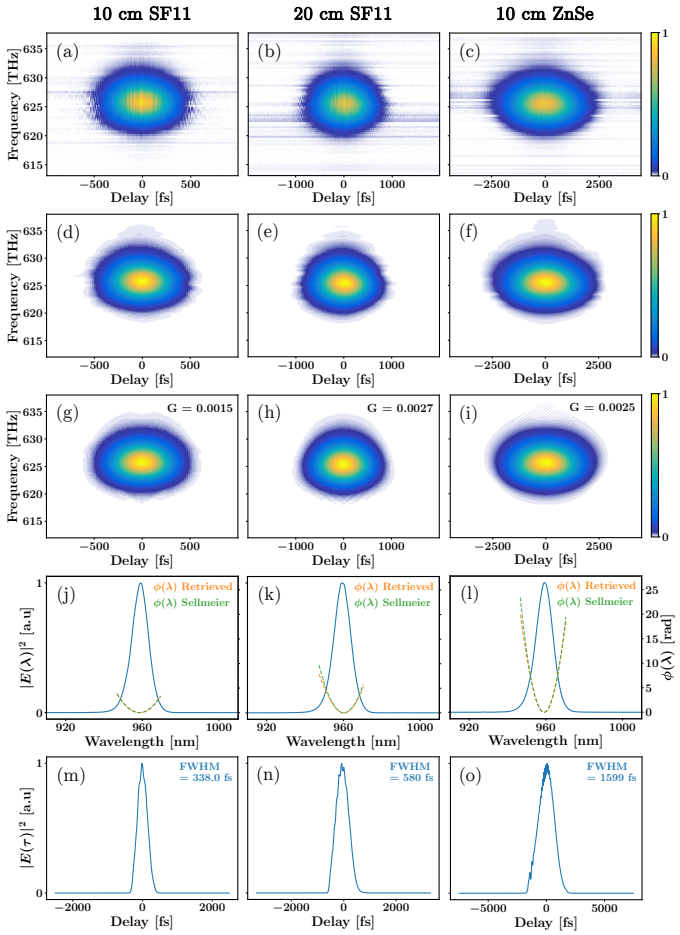

Figure 3.9: **FRACOL-FROG accurately retrieves strongly chirped optical pulses:** We applied FRACOL-FROG to the determination of electric fields for transform limited pulses propagating through 10 cm of N-SF11 glass (left column), 20 cm of N-SF11 glass (middle column), and 10 cm of ZnSe (right column). (a)-(c): Corresponding measured FRACOL-FROG traces. (d)-(f): Fourier filtered traces binned to a 256×256 grid for both N-SF11 traces, and to a 512×512 for the ZnSe trace. (g)-(i): Reconstructed FROG traces, with low FROG G errors indicating successful convergence. (j)-(l): Retrieved spectral intensities and phases. The spectral phases (orange) are compared with the values calculated directly from the Sellmeier coefficients of these materials (green). The agreement is excellent, confirming the accuracy of the FRACOL-FROG method. (m)-(o): Retrieved temporal intensities and FWHM values of the dispersed pulses.

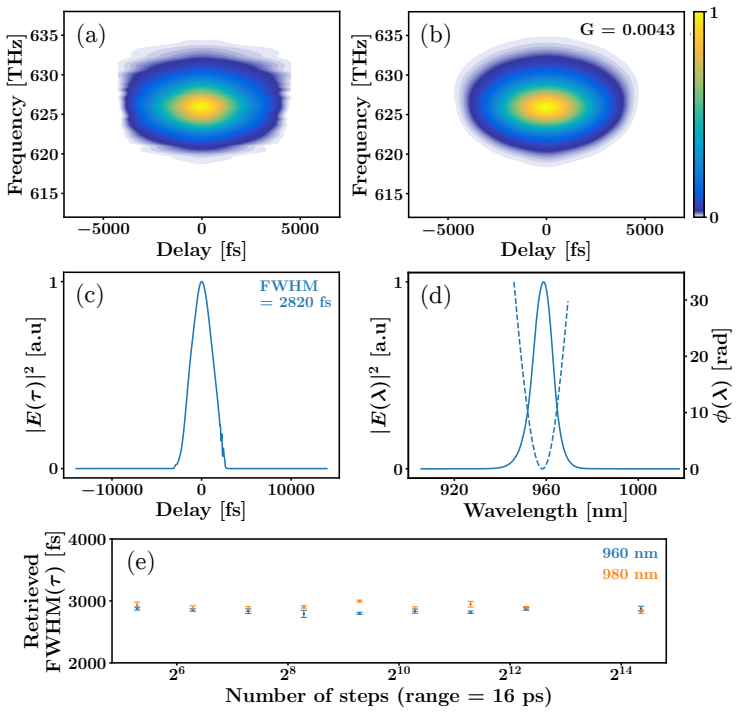

Figure 3.10: **Fast *in situ* characterization using FRACOL-FROG:** The *in situ* measurements were made at the focal plane of a home built nonlinear microscope, shown in Fig. 3.3(b). (a): Measured FRACOL-FROG spectrogram after Fourier filtering. The spectrogram was measured with a spectrometer integration time of 20 ms and a delay step of 0.76 fs. (b): Reconstructed spectrogram after binning to a 1024x1024 grid. (c): Retrieved temporal intensity. (d): Retrieved spectral intensity and phase. (e): Demonstration of the ability of FRACOL-FROG to record reproducible and accurate FROG traces even with fewer delay points. We show the retrieved temporal FWHM by performing FROG scans, at 960 nm and 980 nm, on a scan window of 16 ps with various delay steps (N = 21000,5000,2500,1250,625,312,156,78 and 39). The fields were subsequently reconstructed over a 512×512 grid. The field retrieval is consistent over the entire range with a standard deviation $< 3\%$ of the FWHM value (indicated by the error bars). The great reduction in the needed number of scan steps from Nyquist-resolved 21000 to 39 shows the advantage of FRACOL-FROG for rapid *in situ* laser pulse characterization in nonlinear microscopy.

the system, including double passing five 10 cm-long N-SF11 glass rods, the retrieved pulse duration is 2820 fs. To the best of our knowledge, this is the first time an *in situ* FROG

measurement of such a highly chirped pulse has been reported. Beyond *in situ* measurements, we further demonstrate the utility of FRACOL-FROG in performing rapid FROG scans (fewer delay steps) since the absence of fringes means we are no longer bounded by the Nyquist limit. Though undersampling of cFROG traces was proposed in [35], this was accomplished with a strict condition on the smallest delay step to avoid aliasing. In FRACOL-FROG, averaging out of the fringes enables an undersampling that is immune to aliasing effects. We demonstrate this by performing FRACOL-FROG scans at two different wavelengths (960 nm and 980 nm) over a range of 16 ps, with scan steps ranging from 21000 steps (within the cFROG-required Nyquist limit) to 39 steps, as seen in Fig. 3.10(e). Despite the sparse sampling, FRACOL-FROG enables accurate reconstruction of the electric field, of particular use for highly chirped pulses that span long delay ranges.

One more advantage of FRACOL-FROG making it of particular interest in nonlinear microscopy compared to previous methods relying on type-II phase matching ([37, 38]) is that it removes the requirement for strict polarization purity to achieve fringe suppression. Provided the other FROG conditions including the phase matching bandwidth of the SHG medium are still respected, the NA of the objective should not affect the trace regardless of pulse duration, unlike the previous methods that rely upon high purity polarization [40, 41]. The main limitation we found on objective NA for the FRACOL-FROG method was the limited space in the microscope collection arm for a spectrometer. Therefore, FRACOL-FROG is more robust and easier to implement for nonlinear microscopy settings, particularly in closed commercial microscope systems, than previous cFROG implementations.

3.6 Conclusion

We proposed and experimentally demonstrated a new FROG modality, Fringe-averaged collinear FROG (FRACOL-FROG), which is well-suited to the complete and accurate characterization of shaped optical fields at the focal plane of a laser scanning confocal multiphoton microscope. By using a kHz piezo-driven shaker to dither the path length of one arm of the Mach-Zehnder-like FROG system, we demonstrated accurate FROG retrieval in a collinear geometry using conventional algorithms, which is robust against instabilities arising from interferometric drifts and measurement noise. We additionally showed that FRACOL-FROG allows a reduction in the density of sampling points and is robust to aliasing effects. A limitation of FRACOL-FROG is that it only resolves temporal features broader than the shaker amplitude, making it less applicable to few-cycle pulses that have durations on the order of the shaker's temporal displacement. The same restriction will apply to pulses with narrow temporal satellite pulses. However, for well-behaved longer pulses, we demonstrated that FRACOL-FROG accurately and reproducibly retrieves pulses over a useful range of durations ($\sim$100 fs-3 ps) relevant to multiphoton microscopy modalities such as CRM. We anticipate that the simplicity and collinear geometry of our scheme will be of use in a range of multiphoton microscopies, where the complete characterization of optical fields at the sample focal plane is of significant value. FRACOL-FROG is particularly useful for CM-SRS, where three distinct chirped pulses must be matched to achieve optimal signals, and was used for calibration of the setup described in Chapter 5.

Part II

Background-free SRS microscopy

SRS offers rapid, chemical-specific and label-free imaging, but can often be compromised by non-Raman background signals. Existing optical modulation transfer schemes, based upon linear optical properties, reduce some of these signals but cannot eliminate all of them. Optical phase control of coherent broadband pulses is important in nonlinear optical spectroscopy and microscopy, including in spectral focusing SRS. This nonlinear property provides an opportunity for a new modulation scheme, termed CM. CM-SRS modulates the relative sign but not the magnitude of the linear chirp of the input lasers, leaving all other pulse properties (spectrum, amplitude, polarization, pulse duration) unchanged. This modulation transfer technique removes all non-Raman signals and is linear in both concentration and oscillator strength. CM-SRS yields a quantitative, highly sensitive, background-free Raman signal, making it well-suited to imaging of traditionally challenging samples [10]. Chapter 4 discusses the theory behind CM-SRS and explores methods of improving the protocol for obtaining a spontaneous Raman spectrum from a CM-SRS measurement. Chapter 5 describes an improved experimental implementation of CM-SRS, details the calibration procedure, and outlines future directions for the technique.

4

Chirp modulation - theory

The theory described in the following chapter is largely based on a CM-SRS paper published in 2024 [10], with additional details and clarifications.

4.1 Technique

SRS is free from the non-resonant four-wave mixing background present in CARS, another CRM modality. However, there remain other inherent background effects in SRS that appear as intensity modulations and therefore compete with the Raman signal [10, 11]. These backgrounds can be classified into two main categories: nonlinear absorption and nonlinear scattering [10]. In nonlinear absorption, there is loss in both the pump and Stokes beams. Therefore, with AM, both SRL and nonlinear absorption appear as losses and will have similar lock-in phase responses, making it difficult to distinguish them. Examples of nonlinear absorption processes include two-photon absorption and excited-state absorption [11]. Nonlinear scattering arises when the detector does not collect 100% of the forward propagating signal, appearing as gain or loss and again confusing the detection of a Raman signal. Examples of these processes include cross-phase modulation and thermal lensing [11]. These background signals are sensitive to the intensity and polarization of the input beams, but are generally not strongly chromatic [10]. Importantly, the SRS signal is affected by the spectral resolution (achieved in spectral focusing SRS), whereas the non-Raman background signals are generally not. Therefore, by modulating only the Raman spectral resolution, but keeping all other parameters including the polarization, amplitude, pulse duration and spectrum constant, it will be possible to subtract all non-Raman signals from the SRS response.

In CM-SRS, the Raman spectral resolution is modulated by switching the sign but not

the magnitude of the linear pulse chirp (quadratic phase). In spectral focusing SRS, the spectral resolution is optimal if both the input pump and Stokes pulses are linearly chirped with matching slopes (termed co-chirped) [10, 17]. The opposite case arises when every possible Raman mode, limited by the difference frequency bandwidth of the input pulses, are simultaneously probed. One such configuration is if both input pulses are transform-limited. Another equivalent configuration is if the slope of the linear chirp of one pulse is exactly the opposite sign of the other (termed contra-chirped) [10]. A schematic of the Raman spectral resolution as a function of the sign of the linear chirp is shown in Fig. 4.1(a). By modulating uniquely the sign but not the magnitude of the linear chirp, as

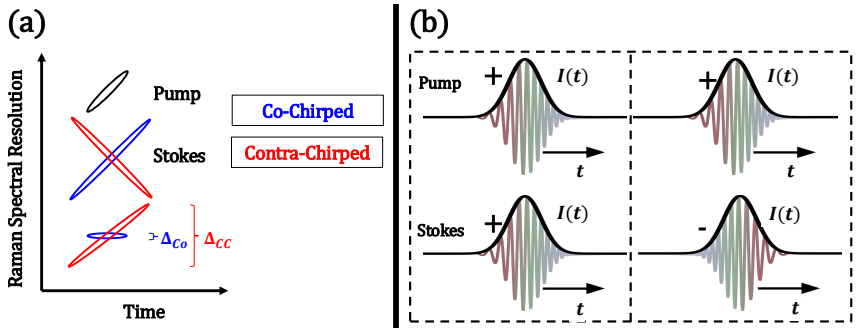

Figure 4.1: **Effect of the chirp sign:** (a): Raman spectral resolution (Δ) for co-chirped (Co)/high resolution and contra-chirped (CC)/low resolution cases. The contra-chirped case is equivalent to both pulses not being chirped whatsoever. (b): Pulses with the same intensity envelope $I(t)$ can be either co- or contra-chirped.

shown in Fig. 4.1(b), it is readily possible to maintain all other pulse characteristics [10].

To create the modulated co- and contra-chirped pair, it is possible to use the same modulation scheme as AM-SRS for the co-chirped beam, and the rejected output for the contra-chirped beam. Importantly, the scan time does not increase, as shown in Fig. 4.2.

As there is still some Raman transfer in the contra-chirped case, the pump beam will still

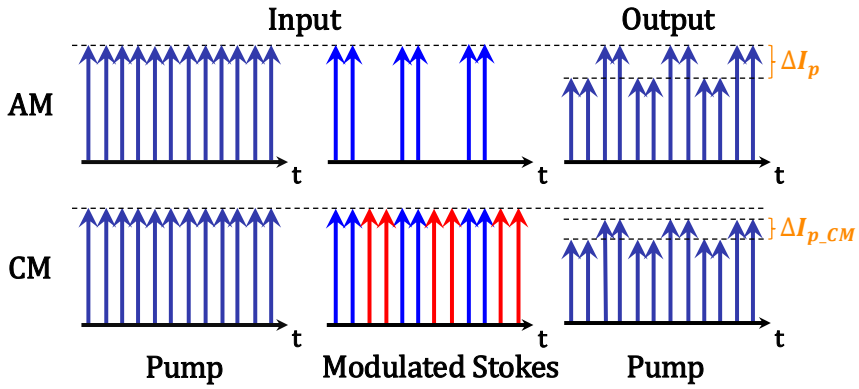

Figure 4.2: **SRS modulation schemes:** AM-SRS is shown on the top. CM-SRS is shown on the bottom, where instead of modulating between a co-chirped beam and nothing, we modulate between high and low Raman spectral resolutions. The detected Raman signal amplitude is denoted by ΔI_p and ΔI_{p_CM}.

undergo loss, though it is much less than the loss with the co-chirped beam. Therefore, for a background-free sample, the CM-SRS signal magnitude is slightly lower than that of an equivalent AM-SRS measurement. Note that in CM-SRS the contra-chirped beam has a very broad spectral response. When multiple Raman modes are present, this can lead to unusual spectral lineshapes when a broad, strong contra-chirped response is subtracted from a weak, narrow co-chirped Raman peak. At certain points in the spectrum, this may result in a local peak that nonetheless has a negative Raman signal amplitude ΔI_{p_CM} globally [10]. Importantly, while this CM-SRS signal is linear in concentration and no deconvolution is necessary to interpret the data, the unusual CM-SRS lineshape can be deconvolved in order to obtain the pure Raman resonant spectral lineshape, as discussed below in Section 4.2.

4.2 Deconvolution

The CM-SRS spectral lineshape is different than that of AM-SRS; though the maxima are at the same location, CM-SRS can give a negative signal at certain points. Importantly, the CM-SRS lineshape may be deconvolved in order to obtain the background-free-equivalent AM-SRS spectrum [10].

4.2.1 Theory

The co-chirped (Co) signal, equivalent to the AM-SRS (AM) spectrum, may be expressed in terms of a convolution ($*$) as follows:

$$S_{Co}(\omega) = S_{AM}(\omega) = G_{Co} * S_{Raman}(\omega) + B(\omega), \tag{4.1}$$

and the contra-chirped (CC) signal as follows:

$$S_{CC}(\omega) = G_{CC} * S_{Raman}(\omega) + B(\omega), \tag{4.2}$$

with S being the signal, G the Gaussian excitation spectrum, B the non-Raman background signal, and ω the frequency. S_{Raman} represents the spontaneous Raman spectrum, typically represented as a Lorentzian resonance. The CM-SRS (CM) signal is equivalent to the

subtraction of the co- and contra-chirped signals:

$$\begin{aligned} S_{CM}(\omega) &= S_{Co} - S_{CC} \\ &= G_{Co} * S_{Raman}(\omega) + B(\omega) - (G_{CC} * S_{Raman}(\omega) + B(\omega)) \\ &= G_{Co} * S_{Raman}(\omega) - G_{CC} * S_{Raman}(\omega). \end{aligned} \tag{4.3}$$

Using first the commutative and then the distributive properties of convolutions, Eq. (4.3) may be expressed as one convolution:

$$\begin{aligned} S_{CM}(\omega) &= S_{Raman}(\omega) * G_{Co} - S_{Raman}(\omega) * G_{CC} \\ &= S_{Raman}(\omega) * (G_{Co} - G_{CC}) \\ &= (G_{Co} - G_{CC}) * S_{Raman}(\omega). \end{aligned} \tag{4.4}$$

In the case where background is appreciable, it is not possible to directly convert the CM-SRS signal into an equivalent AM-SRS signal. However, it is possible to find calibration samples where the Raman dependent term in the AM-SRS signal is much stronger than the background signal. Under this assumption, the AM-SRS signal (termed $AMStrong$) is linearly dependent on the Raman oscillator strength, as expressed below:

$$S_{AMStrong}(\omega) = G_{Co} * S_{Raman}(\omega), \qquad S_{AMStrong} \gg B(\omega), \tag{4.5}$$

as is the CM-SRS signal as demonstrated in Eq. (4.4). In this case, it is possible to convert between the AM-SRS and CM-SRS signals. Importantly, this conversion is related to the

instrument response which is sample-independent. Once this function has been measured for a given instrument, it can be used to deconvolve any CM-SRS signal measured under the same instrument parameters to convert it to the equivalent background-free AM-SRS signal, even in cases where a direct measure of the AM-SRS signal is overwhelmed by background. This deconvolution process is described below.

The convolution theorem relates the convolution of two functions to their Fourier transform F and is defined as follows:

$$F\{u * v\} = U \cdot V, \tag{4.6}$$

with U and V the Fourier transforms of functions u and v. Applying a Fourier transform and the convolution theorem to Eq. (4.5) gives:

$$\begin{aligned} F\{S_{AMStrong}(\omega)\} &= F\{G_{Co} * S_{Raman}(\omega)\} \\ &= F\{G_{Co}\}F\{S_{Raman}(\omega)\}, \end{aligned} \tag{4.7}$$

from which the Raman response S_{Raman} may be isolated:

$$F\{S_{Raman}(\omega)\} = \frac{F\{S_{AMStrong}(\omega)\}}{F\{G_{Co}\}}. \tag{4.8}$$

Substituting Eq. (4.8) into the Fourier transform of Eq. (4.4) gives:

$$F\{S_{CM}(\omega)\} = F\{(G_{Co} - G_{CC})\}\frac{F\{S_{AMStrong}(\omega)\}}{F\{G_{Co}\}}, \tag{4.9}$$

which can be isolated for the strong AM-SRS signal:

$$F\{S_{AMStrong}(\omega)\} = F\{S_{CM}(\omega)\}\frac{F\{G_{Co}\}}{F\{(G_{Co} - G_{CC})\}}. \tag{4.10}$$

We define a sample-independent instrument response function IRF:

$$F\{IRF\} = \frac{F\{G_{Co}\}}{F\{(G_{Co} - G_{CC})\}}, \tag{4.11}$$

which can be replaced into Eq. (4.10):

$$F\{S_{AMStrong}(\omega)\} = F\{S_{CM}(\omega)\}F\{IRF\}, \tag{4.12}$$

or equivalently:

$$F\{IRF\} = \frac{F\{S_{AMStrong}(\omega)\}}{F\{S_{CM}(\omega)\}}. \tag{4.13}$$

The IRF is obtained from the measurement of both the AM-SRS and CM-SRS signals of the same sample in the strong Raman regime and then using Eq. (4.13). Once this is computed, the IRF can be applied to deconvolve any CM-SRS measurement performed under the same parameters via Eq. (4.12).

Isolating for $S_{AMStrong}(\omega)$ gives our final deconvolved CM-SRS signal:

$$S_{AMStrong}(\omega) = F^{-1}[F\{S_{CM}(\omega)\}F\{IRF\}] = D_{CM}, \tag{4.14}$$

with D_{CM} representing the deconvolved CM-SRS spectrum that is equivalent to the background-

free SRS response, which in the field of SRS is often approximated to be equivalent to the spontaneous Raman spectrum.

4.2.2 Deconvolution limits

While the deconvolution process using Eq. (4.13) and Eq. (4.14) works on ideal CM-SRS data with no noise, it is well-known that deconvolution can magnify noise and have limits in real experimental settings [54]. To characterize practical limits and develop mitigation strategies for the deconvolution of CM-SRS spectra, we simulated the workflow using those equations under three conditions: undersampling; additive noise; and additive noise followed by smoothing with a rolling-average window function. The results are summarized in Fig. 4.3.

We used a simulated dimethyl sulfoxide (DMSO) SRS spectrum with peaks centred at 2913 cm^{-1} and 2993 cm^{-1}, with the fully sampled dataset containing 501 points. To numerically undersample, we retained 50%, 20% and 10% of the points for the simulated measured CM-SRS spectrum, with the 10% case barely resolving peaks in the raw measured data. In all cases, the deconvolution recovered the peak structure reasonably well, producing spectra resembling the strong AM-SRS spectrum, as seen in Fig. 4.3(a).

To model experimental conditions, we added 10% additive noise to one spectrum of either the strong AM/CM reference or the simulated measured CM spectrum at a time. Depending on the exact form of the noise, the deconvolution sometimes produced very noisy outputs. Fig. 4.3(b) shows example cases where the deconvolution failed when the

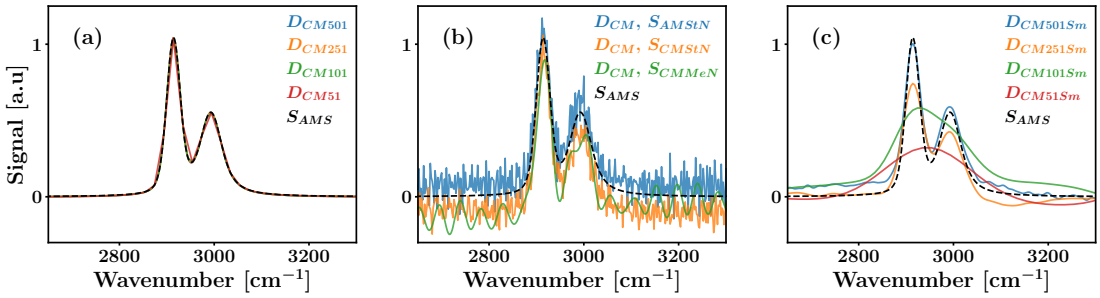

Figure 4.3: **CM deconvolution limits:** Simulated deconvolution of CM-SRS spectra (D_{CM}) under different experimental conditions. S_{AMS} (black dashed line) represents the strong AM-SRS spectrum that the deconvolution should theoretically match. (a): Deconvolution at different sampling densities, $D_{CM\#}$, # representing the number of sampled steps. Even at lower densities, where the peaks start to lose resolution, the deconvolution still gives results that resemble the theoretical curve. (b): Example deconvolution under presence of noise (N) in one of either the strong AM-SRS (AMStN), strong CM-SRS ($CMStN$), or measured CM-SRS ($CMMeN$) spectra. The deconvolution can sometimes amplify the noise under these conditions. (c): Example deconvolution where a spectrum containing noise (N) was smoothed (Sm) using a rolling-average window, at different sampling densities $D_{CM\#}$. The deconvolution works well for oversampled data, but undersampled data loses spectral resolution due to the smoothing.

measured CM-SRS spectrum was noisy, though similar behaviour can occur when any of the required inputs for calculating the instrument response function are noisy. This is consistent with the known behaviour of deconvolution to amplify noise [54].

Because smoothing attenuates high-frequency noise, though at the expense of resolution [54], we next applied a rolling-average windowing function to the noisy input data and verified the effect on the deconvolved spectrum. As seen in Fig. 4.3(c), smoothing can improve the robustness of the deconvolution in the presence of noise. However, smoothing will also broaden peaks, potentially reducing spectral resolution. Oversampled peaks were less susceptible to broadening by the windowing function, but as the peaks were progressively undersampled, the final achievable spectral resolution was noticeably

degraded due to the smoothing required. This trade-off is shown in experimental data (Fig. S6 in the original CM-SRS paper [10]), where the deconvolution of a CM-SRS pine stem spectrum blurs finer features that could be seen in the original CM-SRS data. To benefit from smoothing while not compromising spectral resolution, the recommendation is to greatly oversample the original measurement, apply gentle smoothing to stabilize the deconvolution, thereby preserving effective resolution after deconvolution. Alternatively, reducing the noise in the various input spectra, via averaging for example, could improve the stability of the deconvolution process. The major downside of both oversampling and increased averaging is the increased exposure time required, which can lower throughput and increase the chance of phototoxic effects in living systems.

5

Chirp modulation - Experimental Implementation

This chapter describes an improved experimental implementation of CM-SRS, details the calibration procedure, and outlines future directions for the technique.

5.1 Experimental setup

We built a second-generation CM-SRS setup based on the original [10] with improved chirp control. For this, we designed and implemented a transmission grating stretcher/compressor pair and calibrated the system using our FRACOL-FROG device, leading to several key improvements. Our setup was designed for optimal power efficiency to allow for higher-power imaging of material samples. Additionally, the new design allows for maximizing background cancellation by (i) reducing heating effects in the grating compressor that can lead to spatial mode mismatch and (ii) by as closely as possible matching the chirp magnitudes of the co- and contra- chirped beams by allowing for easy dispersion tunability. This setup may also be used as an AM-SRS setup, similar as described in [55, 56], simply by blocking the contra-chirped beam before recombination with the co-chirped beam.

The experimental setup is depicted in Fig. 5.1. Both outputs of a dual output femtosecond laser system (Insight X3, Spectra-Physics) are used. The tunable beam (680 nm-1300 nm) is expanded with a 1:3 telescope, and attenuated using a HWP-PBS combination with a motorized rotation stage (PR50CC, Newport). Next, it goes to a 20 cm-travel variable delay stage (ILS200CC, Newport) to allow the rapid spectral scanning of the system. It is chirped by double-passing three 10 cm-long N-SF11 rods (SF11L1100-AR800, Newlight), equivalent to approximately 1.7 ps duration for 960 nm as computed from the known Sellmeier coefficients of this standard optical material [50]. It then passes through a 5:4 telescope to match the diameter of the fixed-wavelength laser beams, and a 1:1 telescope

where a spatial filter can easily be added and that gives control over the beam divergence. Finally, it undergoes extra path length travel required to overlap in time with the fixed beams, passes through a polarizer-HWP-quarter-wave plate (QWP) polarization compensator, and is sent through a dichroic mirror (NF1064-44, Thorlabs) to permit recombination with the fixed beams.

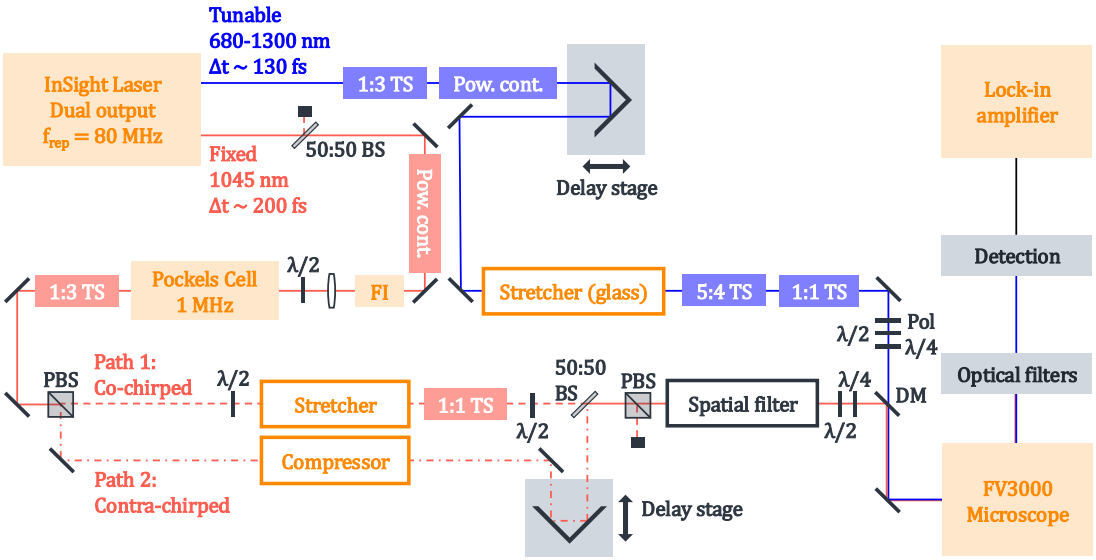

Figure 5.1: **Experimental setup for CM-SRS:** The tunable output is variably delayed, chirped using N-SF11 glass, and recombined with the fixed beam and sent to the microscope. The fixed beam is modulated at 1 MHz and split into the co- and contra-chirped beams. The two fixed beams are chirped with opposite signs using Martinez grating stretcher and compressors. They are finely controlled with a 1:1 telescope, a motorized HWP, and a delay stage so as to perfectly match their spot sizes, divergences and time delay. They are recombined and passed through a polarizer that matches their polarization and allows for fine power control to balance their powers, and then a spatial filter that overlaps them in space. They are recombined with the tunable beam and sent into the microscope. TS, telescope; Pow. cont., power control; Pol, polarizer; $\lambda/2$, HWP; $\lambda/4$, QWP; BS, beam splitter; FI, Faraday isolator; PBS, polarizing beam splitter; DM, dichroic mirror.

In our lab, the fixed beam (1045 nm) is split at a 50:50 beam splitter (032-7450P,

Eksma) to allow a second setup to use half the power, but this is not a requirement. Next, it undergoes further variable attenuation with a HWP-polarizer combination. It is then sent through a Faraday isolator (IO-3-1064-HP, Thorlabs) to prevent back reflections into the laser, and is collimated with one long focal length lens. The polarization is set with another HWP, and then the fixed beam modulated with a Pockels Cell (M360-160, Conoptics) at 1 MHz with a square wave from a function generator (RIGOL model DG822). Next, it is expanded with a 1:3 telescope, and split into the co- and contra-chirped beam pair by a PBS. The co-chirped beam is stretched and the contra-chirped beam is compressed using a tunable single-pass folded Martinez transmission grating system [57], described in detail in Section 5.1.1. The co-chirped beam passes through a HWP to match it to the incident polarization of the gratings (T-1600-1030s-31.8x24.8-94, LightSmyth). The co-chirped beam goes through a 1:1 telescope to allow for correcting unmatched divergences, and then a HWP on a motorized stage (PR50CC, Newport) that will allow for fine matching of the co- and contra-chirped beam powers. Meanwhile, the contra-chirped beam is sent to a fine-control motorized linear stage (E-873, PI) which allows for exact matching of the time delay between the two beams. The two fixed beams are recombined with a 50:50 beam splitter (032-7450P, Eksma), sent through a PBS to match in polarization and to allow power control of the co-chirped beam, and sent through a spatial filter comprised of a 1:1 telescope and a 100μm pinhole. The beam is then passed through a HWP-QWP combination for polarization compensation with the previous PBS. Finally, it is reflected off the dichroic mirror to be recombined with the tunable beam. The recombined beams are then introduced into the microscope.

All microscope measurements were performed using a custom multimodal nonlinear microscope (FV3000 Confocal Microscope, Evident). The incoming light was focused using a 20x 0.8 NA objective (UPLXAPO20X, Evident). Backwards non-descanned measurements were detected using an external photomultiplier tube (PMT) (H10723-210, Hamamatsu), with the signal sent directly to a lock-in amplifier (UHFLI, Zurich Instruments). The beam for the forward direction SRS measurements was collected using a 25x 1.05 NA water immersion objective (XLPLN25XWMP2, Evident), filtered with two fluorescence filters to block the Stokes (FF01-850/310-25, Semrock), and detected using a photodiode (S3590-08, Hamamatsu). The details of the electronics for SRS measurements are explained here [56].

5.1.1 Transmission Grating Assembly for Dispersion Control

To control the temporal dispersion of the beams, we used a folded single-pass Martinez configuration grating stretcher/compressor. A Martinez configuration is a grating stretcher that uses a 1:1 telescope after the first grating to collimate the beam and allow for either positive or negative group-velocity dispersion (GVD) to be applied to the beam [57–59]. A reflective Martinez configuration allows for the stretched and compressed beams to be perfectly matched in all but chirp sign [59], and a transmission Martinez configuration will be nearly matched. This makes a Martinez configuration ideal for use in CM [10]. A single-pass grating stretcher is defined as the beam being dispersed and collimated by gratings one time each (two total passes through gratings). This configuration has the advantage of simplicity and being more power efficient, but at the cost of residual collimated horizontal

spatial chirp. A double-pass grating stretcher will have the beam contact the gratings four times in total. This configuration has no residual horizontal spatial chirp, but will be less power efficient [57, 60, 61].

To optimize tunability, power efficiency, and space constraints, we built a folded single-pass Martinez transmission grating stretcher as described in Fig. 5.2 [60]. The transmission gratings (T-1600-1030s-31.8x24.8-94, LightSmyth) had 1600 lines/mm and were designed for 94% efficiency at 1030 nm. The focusing cylindrical lens (LJ1996L1-B, Thorlabs) was of 300.12 mm focal length and 2" wide to accommodate the highly dispersed beam. The beam was folded using a 2" wide×1" tall retroreflector (RM-102-5E, PLX). Both the lens and the retroreflector are on fine-tuning manual linear translation stages to allow for chirp tunability. The beam returns through the same optics at a lower height and is picked off using a D-shaped mirror.

The choice of a long focal length lens was made for three main reasons. The first reason was to minimize the horizontal spatial chirp associated with single-pass grating stretchers. A long focal length lens will have a longer Rayleigh length z_R, defined for a Gaussian beam as [62, 63]:

$$z_R = \frac{\pi \omega_0^2}{\lambda}, \tag{5.1}$$

with ω_0 representing the beam waist (the beam radius at the smallest point) and λ representing the wavelength. In the paraxial approximation, the beam waist will be proportional to the focal length [63]:

$$\omega_0 = \frac{\lambda f}{\pi \omega}, \tag{5.2}$$

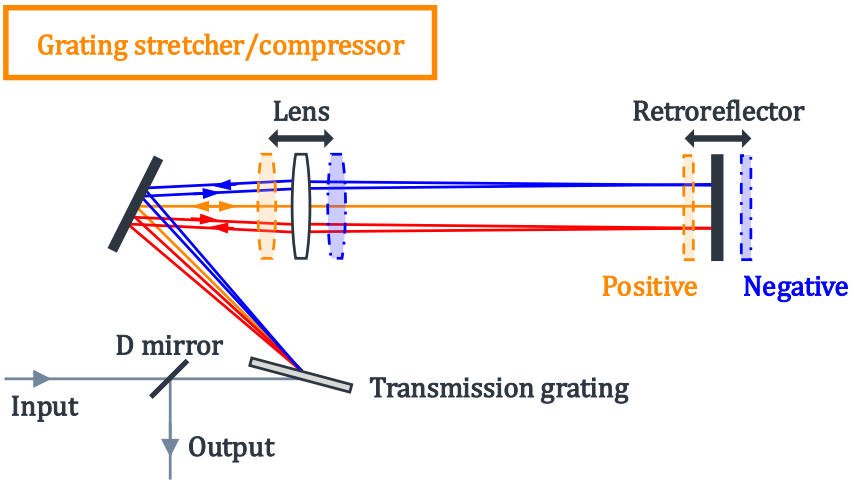

Figure 5.2: **Folded single-pass Martinez transmission grating stretcher:** A Martinez grating stretcher comprises a 4f-setup that has a zero-dispersion configuration (black) as shown. Tuning the lens-retroreflector pair together will introduce an optical path length difference between the red and blue-shifted colours, imprinting negative (blue configuration) or positive (orange configuration) dispersion on the pulse. The retroreflector mirror folds the setup, allowing for using only one grating instead of two, and lowers the height of the returning beam at a parallel output angle, allowing for easy picking off of the output beam.

with f the focal length and ω the beam diameter of the collimated beam. Combining Eq. (5.1) and Eq. (5.2) gives:

$$z_R = \frac{\lambda f^2}{\pi \omega^2}, \tag{5.3}$$

meaning that as f increases, z_R increases too. We chose to use a single-pass system for simplicity and for optimal power efficiency, which means horizontal spatial chirp will be present. This effect will be minimized if the displacement from the tightest focus that we will be doing to tune the stretchers is within the Rayleigh length, therefore we want to maximize the focal length. The second reason for choosing a long focal length is for ease of alignment. With the longer Rayleigh length, the displacement of the lens-retroreflector

pair from the grating can be less precise while still giving the same dispersion. Finally, a larger beam waist means that there will be a lower power load at the focus on the mirror surface, which is the ideal scenario for increased thermal stability of the system. The lens focal length is ultimately limited by the lenses and retroreflectors available for purchase, and by available table space for the stretcher and compressor.

To easily pick off the output beam of the folded grating stretcher, the beam must return at a different height. This height change must be done with a retroreflector or another mirror configuration that will return the beam at an angle parallel to the incident beam and perpendicular to the face of the grating. If instead of the return beam being parallel, it was reflected with a mirror at a tilt, this will cause the beam to cross the grating at a tilted angle. This will create uncompensated vertical angular dispersion in the output beam, which will induce spatial chirp and affect the pulse duration and beam divergence [64, 65]. This is particularly not suitable in CM-SRS, where we want two beams that are identical in every way other than the sign of their chirp, and so we do the height change with a retroreflector.

When setting the stretcher and compressor, first the lens and retroreflector are set at one focal length apart. The next step is to set the pulse durations of same magnitude but opposite chirp signs, we used the FRACOL-FROG to do so. To change the pulse duration, the lens-retroreflector pair must move together. The chirp is positive if by taking steps towards the grating, the pulse duration gets longer; and the chirp is negative if by taking steps towards the grating, the pulse duration gets shorter. Alternatively, a mildly dispersive element such as a rod of N-SF11 glass could be placed in the beam to stretch the beam and

to see if the beam increases or decreases in pulse duration after doing so. With our setup, adjustments of 0.5 mm are appropriate for this coarse chirp matching step. To account for the effect of the internal microscope components on the chirps, fine chirp matching must be done at the microscope focal plane. Either FRACOL-FROG measurements or cross-correlations in fluorescein can be used for this step. The steps for fine chirp matching are explained in Section 5.2 as this step will need to be repeated regularly to ensure optimal balance of the co- and contra-chirped beams.

5.2 Calibration

For high-quality, reproducible data that is free from artifacts, the instrument should be calibrated regularly. The procedure that follows ensures that: 1) the co- and contra-chirped beams have identical chirp magnitudes, 2) the co- and contra-chirped beams are spatially overlapped, 3) all the beams are synchronized in time, and 4) the powers are balanced at the sample plane. If the microscope is significantly out of calibration, this procedure may not be sufficient and additional alignment steps may be necessary.

For the whole calibration, we will measure an *in situ* temporal cross-correlation signal in an external PMT with no realignment; to do so in our microscope we measure nondegenerate two photon fluorescence in fluorescein in the backwards direction on the non-descanned detection configuration. In running a temporal cross-correlation in this configuration, we will collect a Gaussian-profile spectrum. We run three scans, one with the co-chirped beam and the tunable (the co-chirped scan), one with the contra-chirped

beam and the tunable (the contra-chirped scan), and one with all three beams (the CM scan). With the lock-in phase set to maximize the signal of the co-chirped beam, if the co- and contra-chirped beams are perfectly balanced, the individual beam scans will produce identical but opposite-sign Gaussian signals, and the CM scan will produce a zero signal. The goal of the calibration is to get as close to that condition as possible.

To first ensure the chirp magnitudes are matched, we fit the cross-correlations of the co- and contra-chirped scans to a Gaussian, and ensure they have the same FWHM to within 1%. If the chirp magnitudes have drifted, we adjust one stretcher by moving the micrometer of both the lens and the retroreflector by the same distance. Steps of 0.05 mm should be sufficient for fine chirp matching. For the co-chirped beam, moving the pair towards the grating will give a longer pulse. For the contra-chirped beam, moving the pair away from the grating will give a longer pulse. Any steps in the path length of the grating stretchers made during chirp-matching should be compensated with the fine-tuning delay stage.

The next step is to ensure the co- and contra-chirped beams are perfectly spatially overlapped. To do so, we look at the field of view in the microscope with a colour map that assigns one colour to the positive signal and another to the negative signal, as seen in Fig. 5.3. If the two beams are not well spatially overlapped, the field of view will have clear colour separation, but if they are, the colours will be roughly equally dispersed across the whole field of view. To achieve ideal spatial overlap, we use the last independent mirror to make small adjustments to the beam that has the 1:1 telescope.

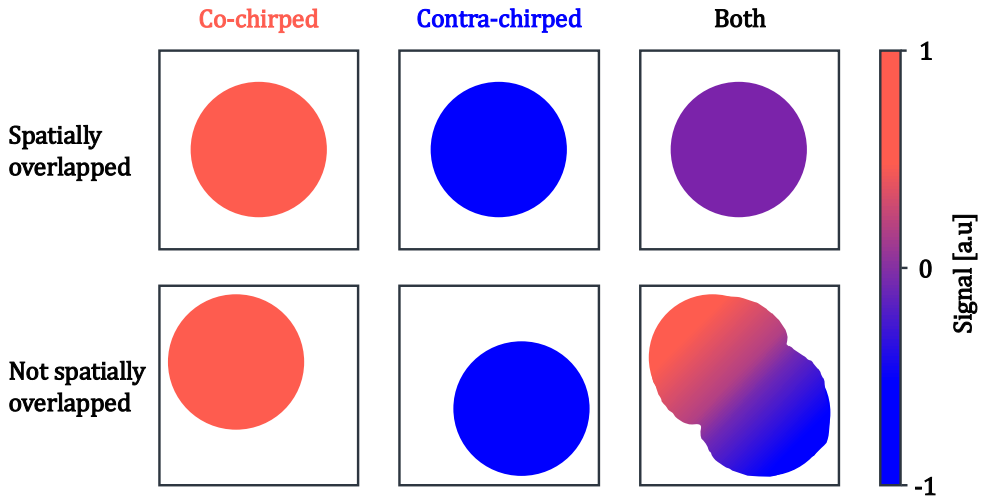

Figure 5.3: **Example CM calibration - spatial overlap:** The microscope field of view is represented using a diverging colour map with red assigned to the positive (co-chirped) signal and blue assigned to the negative (contra-chirped) signal. If the beams are well spatially overlapped (top row), they will be nearly indistinguishable when both are on the sample plane. If they are not spatially overlapped (bottom row), they will be distinguishable with each favouring a different part of the field of view.

Once the beam alignment is set, we check the temporal overlap of the co- and contra-chirped beams. A demonstration of this procedure is shown in Fig. 5.4. The temporal positions of the co- and contra-chirped cross-correlations will shift based on their relative delay as seen in Figs. 5.4(a)-(b). If the co- and contra-chirped beams are overlapped in time, the subtraction of their cross-correlations will yield a Gaussian-shape in much smaller intensity, or for the normalized signal, a near-zero curve, see the blue curve in Fig. 5.4(c). If the beams are not perfectly overlapped in time, the subtraction of their normalized signals will yield a sin-like shape instead of a Gaussian, see the orange curve in Fig. 5.4(c).

Finally, the powers of the co- and contra-chirped beams must be balanced. Again

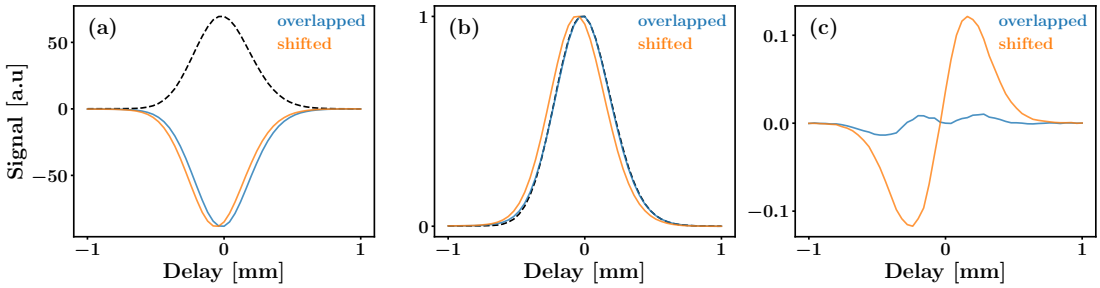

Figure 5.4: **Example CM calibration - time delay:** Example calibration for temporal overlap using cross-correlation scans of the tunable beam with one fixed beam, black dashed line = co-chirped scan; blue line = contra-chirped scan at overlapped time; orange line = same contra-chirped scan shifted by one step (0.04 mm). (a): Measured curves, amplitudes are different and will be corrected via power balancing in the next step. (b): Normalized curves, where the blue curve is well overlapped in time with the co-chirped beam and the orange curve is clearly shifted. (c): Subtraction co−contra normalized scans, with the overlapped case oscillating around zero, and the shifted case clearly in a sin-like shape, indicating its temporal overlap should be improved.

running the cross-correlations, we check if the non-normalized curves of the co- and contra-chirped scans subtract each other. If the co-chirped beam is favoured, we reduce the power of the co-chirped beam, and if the contra-chirped beam is favoured, we increase the power of the co-chirped beam by tuning the angle of the motorized HWP in the co-chirped beam path. Once this balance is close, we run some CM cross-correlation scans and ensure that the resulting signal is essentially zero, with a similar shape as the blue curve in Fig. 5.4(c). It is also theoretically possible to perform this step by stepping the tunable beam to the point of maximal intensity in the cross-correlation scan (time-zero), increasing the time constant in the lock-in to the order of miliseconds, and adjusting the power balance to zero out the average signal. However, in our setup there is some polarization leakage from the Pockels cell, leading to small interference effects that complicate balancing the powers without performing the cross-correlations. A discussion on this leakage and potential

solutions is found in Section 5.4.

5.3 Results

We successfully calibrated the system following the steps described in Section 5.2. The co- and contra-chirped beams were matched in chirp magnitude, overlapped in time, and balanced in powers, providing CM measurements that effectively cancel out the fluorescent signal of the cross-correlation. The steps of this successful calibration procedure are shown in Fig. 5.5. While it is difficult to achieve perfect cancellation in the system due to interference effects, which are touched on in Section 5.4, it is still possible to perform CM-SRS measurements using a nearly-ideal calibrated system that we obtain from these steps, ending up with cancellation that resembles the green case in Fig. 5.5(d).

To ensure the functionality of the setup and the sensibility of the traces, we performed measurements of DMSO diluted in H_2O at two different concentrations (10% and 3%) as seen in Fig. 5.6. These results show good agreement with the original CM-SRS data [10]. For AM-SRS measurements, as the concentration decreases, the peaks, especially the smaller peak at 2993 cm^{-1}, become less distinguishable because the signal starts to be overwhelmed by non-Raman backgrounds [10]. For CM-SRS measurements, the peaks remain visible and distinct even as the concentration decreases. The CM-SRS signal is also quantitative, with the peak heights for the 3% concentration at approximately one third of those of the 10% concentration. A background-free AM-SRS spectrum may be recovered from the CM-SRS data by performing a deconvolution.

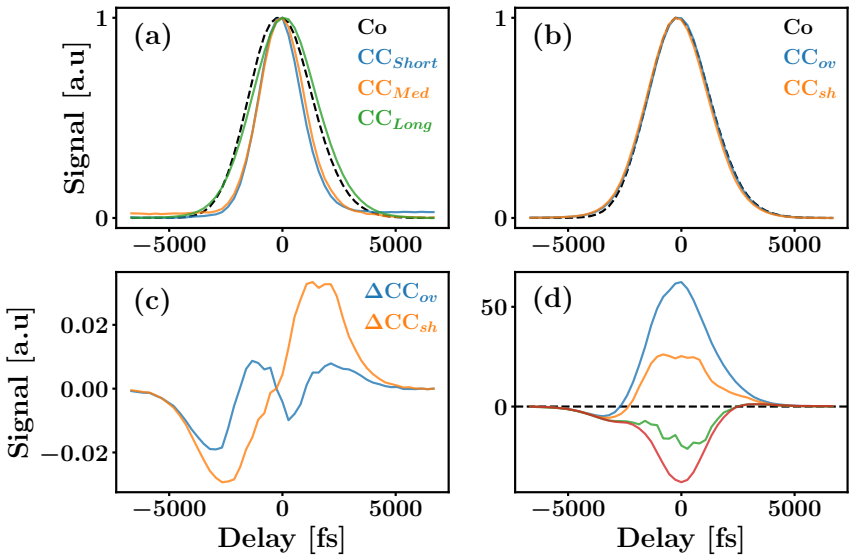

Figure 5.5: **Successful CM-SRS calibration:** The full experimental calibration process is shown in order. (a): Chirp-matching the contra-chirped (CC) beam (coloured lines) to the co-chirped beam (black dashed line), normalized. The green case is of the same width as the co-chirped beam within 1%, meaning the chirps are matched, but the relative pulse delays remain to be set. (b): Time overlap, normalized, where the blue overlapped case CC$_{ov}$ coincides with the co-chirped beam, while the orange case CC$_{sh}$ is slightly shifted. (c): Time overlap, difference between the normalized co-chirped beam and the two contra-chirped beam cases from (b). The behaviour is the same as that described in Section 5.2. (d): Power matching using CM fluorescent scans. The green case has the lowest amplitude, therefore we consider this case to be power-matched.

5.4 Potential improvements

Although the system is working well, several modifications would simplify alignment and calibration and improve balancing of the co- and contra-chirped beams. The first area of improvement is related to the alignment of the tunable beam. Currently, the tunable beam exhibits a wavelength-dependent lateral pointing shift originating in the laser cavity

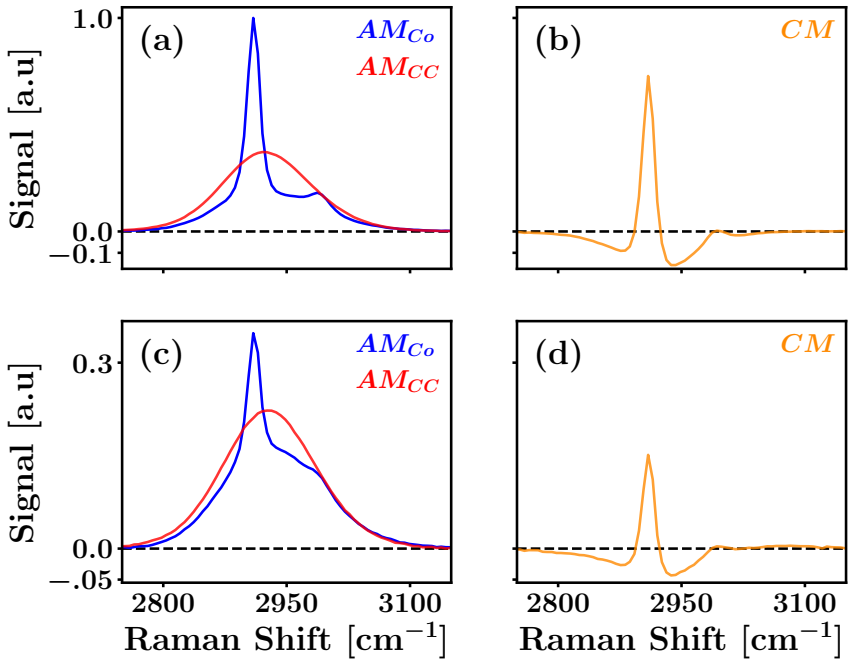

Figure 5.6: **Comparison of AM-SRS and CM-SRS of DMSO in D_2O:** Co-chirped/AM-SRS (AM_{Co}, blue), contra-chirped (AM_{CC}, red), and CM-SRS (CM, orange) scans of DMSO in H_2O at 10% concentration ((a), (b)) and 3% concentration ((c), (d)). CM can be approximated as $AM_{Co} - AM_{CC}$. At lower concentrations, AM starts to be overwhelmed by background, but the CM peaks remain visible.

at shorter wavelengths that displaces the beam from the preferred optical alignment. As a result, it is not possible for a measurement to cover both the fingerprint ($\approx 870 - 1010$ nm for a 1045 nm Stokes beam) and the C-H stretch ($\approx 780 - 820$ nm for a 1045 nm Stokes beam) ranges without realigning the beams. To improve this, we plan to implement an automatic pointing stabilizer on the tunable arm to correct lateral pointing shifts out of the laser, enabling seamless switching between the fingerprint and C-H stretch regions without realignment.

Another area of improvement is the alignment of the external non-descanned PMT that we use for CM calibrations as described in Section 5.2. Currently, this port does not have the same alignment as the forward-direction ports. Because calibrations should reflect the same alignment used for CM-SRS measurements, this means that the calibration in the non-descanned PMT is done off-centre, preventing the assessment of the spatial overlap in the lower half of the beams. To ensure the calibration and measurement share the same alignment, the beam should first be aligned in transmission, and the non-descanned PMT assembly physically translated until the beam is also centred in the non-descanned direction.

The largest opportunity for improvement concerns small but noticeable interference effects in our calibration caused by the polarization impurity and leakage from the Pockels cell. The Pockels cell (M360-160, Conoptics) specifies a contrast ratio of 100:1, so approximately 1% of the beam leaks through the other stretcher configuration and arrives temporally coincident with the desired beam at the sample. Because the two configurations are otherwise designed to be identical, this leakage effectively forms an unintended interferometer. As discussed at length in Chapter 3, interference effects make a system much more sensitive to small drifts. In CM-SRS, we require equal powers in the co- and contra-chirped beams; however, if the beams lie on a fringe, this power balance can vary with very small drifts. To mitigate this, it would be possible to take a similar approach to FRACOL-FROG and average out these fringes via optical path length dithering. This could be done in many ways, including a piezo-driven retroreflector or an electro-optic phase modulator inserted in one arm.

Finally, due to these interference effects, the CM-SRS power balancing is sensitive to air currents. Therefore, the system is most stable when the enclosure around the optical setup remains closed. Presently, the enclosures must be opened to block and unblock the co- and contra-chirped beams both when trying to perform our calibrations and when toggling between AM-SRS and CM-SRS scans. To avoid creating these currents, we propose replacing the manual beam blocks with motorized shutters in each arm. This will make switching between the co- and contra-chirped beams easier and minimize fluctuations in the power balance.

5.5 Future directions

Histopathology has long been an important tool in cancer diagnosis [66, 67]. A standard method of performing histopathology is through fixing or frozen sectioning and staining with hematoxylin and eosin (H&E) labels. H&E staining is used to distinguish cellular structures and identify cell and tissue types [67, 68]. H&E staining is the most commonly used method in tumour diagnosis, and these samples are routinely archived [67]. More recently, there have been efforts to digitize these samples and use deep learning and artificial intelligence (AI) to aid in image preprocessing and segmentation, with promising results [69].

Another area of advancement in histopathology has been in using SRS microscopy to perform label-free histopathology measurements in a technique called Stimulated Raman histology (SRH). The first SRS measurements for brain tumour identification were done in

freshly extracted, unprocessed tissue, and the Raman spectrum provided chemical contrast between healthy and cancerous cells [70], with *in vivo* measurements demonstrated shortly after [71]. SRS is particularly advantageous due to its quantitative nature [71]. In SRH, images are segmented ("virtually stained") in a way to mimic the behaviour of traditional H&E staining, allowing SRH images to stand in as H&E stained samples [70–73]. SRH is not only label-free, but can be performed *in vivo*, allowing for a quicker procedure and being of particular use in surgical settings. In view of this, clinical devices for SRH were developed that can perform intraoperative measurements, allowing for real-time analysis by clinicians [73]. Other studies on SRH have focused on using unstained samples from tumour banks to develop the technique [74]. Another advantage of SRH is that the non-destructive and stain-free nature of the technique preserves the genomic integrity of the sample, so information on molecular genetics that are essential in classifying certain types of tumours can be extracted from the same sample [74–76].

To improve diagnosis speed and reliability, AI has been integrated with SRH in a method known as Intelligent Histology [76, 77]. The quantitative nature of SRH is an extra dimension that is not present in traditional H&E staining and that can help train large-scale SRH-AI models for cancer diagnosis. In a clinical trial of Intelligent Histology, the model showed the same accuracy as human patholologists, but came to a diagnosis in a fraction of the time [76].

There are several reasons why it could be of interest to perform SRH measurements on archival samples already stained with H&E. A big reason is in having a larger training dataset for Intelligent Histology AI approaches. In general, extracting new samples is

a labour-intensive and time-consuming process [70, 73], and samples of certain types of tumours can be rare and in high demand [74]. However, if there was a method of recording SRH images on existing samples that happen to already be stained, then the training dataset could be significantly expanded at a much reduced cost compared to harvesting new samples, and without needing to deplete limited quantities of unstained rare tumour samples. A second reason is SRH offers additional quantitative markers beyond traditional H&E staining. Applying SRH to previously stained archival samples that already exist in vast quantities could yield new molecule-specific biological insights unobtainable at the time of original collection.

To date, SRH of previously H&E-stained samples has not been reported. The dyes and mounting media introduce strong background signals that could dominate the SRS response [78, 79]. However, CM-SRS can suppress fluorescence and these other backgrounds. Our goal is to leverage CM-SRS to enable SRH of archival H&E-stained slides, unlocking the use of these archival samples for quantitative, label-free SRH analysis.

Beyond applications in stained tissue imaging, CM-SRS has many other potential uses. One example is in imaging micro- and nanoplastics in the environment. Currently, microplastics detection is largely confined to particles several microns in size, despite the biological impact of nanoplastics. Additionally, many environmental plastics are naturally fluorescent due to weathering and have strong background signals, limiting the ability to chemically identify them via spontaneous Raman or standard SRS microscopy [80, 81]. CM-SRS could allow the biologically important smaller (sub-micron) nanoplastics to be imaged in a background-free manner, allowing them to be chemically identified. Other

media traditionally challenged by background signals in SRS microscopy include plant materials [10, 11, 82], pigmented skin tissue [11, 15] and mineralogical samples [56, 83, 84], for which CM-SRS microscopy could substantially facilitate imaging [10]. As we go forward with our new CM-SRS system, we aim to tackle many of these important issues.

6

Conclusion

Motivated by the advantages of CM-SRS over conventional SRS techniques, in this work we designed a constructed a second generation CM-SRS microscopy facility. The first step involved building a FROG pulse characterization device suitable for performing *in situ* measurements of our chirped pulses for spectral focusing SRS. We termed this device FRACOL-FROG, and it is based upon fringe removal via optical path length dithering [22]. FRACOL-FROG increases the robustness of the cFROG scan to interferometric drift

instability, allows for undersampling of typically dense measurements, and is compatible with conventional SHG-FROG algorithms. The ability to undersample is particularly advantageous for pulses that are significantly chirped, such as those frequently used in spectral focusing SRS microscopy. We anticipate that the simplicity and collinear geometry of our scheme will be of use in a range of multiphoton microscopies.

We then implemented a new design for CM-SRS, a Raman modulation transfer technique that relies on modulating the linear chirp, a nonlinear optical property, to achieve Raman contrast. The CM-SRS spectrum is free of non-Raman backgrounds and is linear in oscillator strength and concentration [10]. The previous implementation was limited in total power throughput due to the use of metallic reflection gratings, which could also distort the spatial mode of the beams. Additionally, the use of both glass and gratings to chirp the beams made it challenging to achieve matched chirps as required for CM-SRS. Using the FRACOL-FROG device to calibrate the new system, it is now operational and able to record high spectral resolution CM-SRS spectra. However, there remain opportunities for further improvement. The system suffers from interference-induced instabilities between the co- and contra-chirped beams. This could potentially be mitigated using optical path length dithering in a similar idea to our FRACOL-FROG approach, and will be tested in the future. Beyond technical refinements, the system is poised to deliver high-resolution, background-free, chemical-specific, and high-sensitivity CM-SRS measurements across a range of important and previously challenging samples. In particular, we envision its application to archival stained biological samples to provide new insights for health analytics.

References

1. Toseland, C. P. Fluorescent labeling and modification of proteins. Journal of Chemical Biology **6,** 85–95 (2013).
2. Wei, L. & Min, W. Electronic Preresonance Stimulated Raman Scattering Microscopy. The Journal of Physical Chemistry Letters **9.** PMID: 30001137, 4294–4301 (2018).
3. Evans, C. L. & Xie, X. S. Coherent Anti-Stokes Raman Scattering Microscopy: Chemical Imaging for Biology and Medicine. Annual Review of Analytical Chemistry **1,** 883–909. ISSN: 1936-1335 (2008).
4. Nie, S. & Emory, S. R. Probing Single Molecules and Single Nanoparticles by Surface-Enhanced Raman Scattering. Science **275,** 1102–1106 (1997).
5. Schellenberg, P., Johnson, E., Esposito, A. P., Reid, P. J. & Parson, W. W. Resonance Raman Scattering by the Green Fluorescent Protein and an Analogue of Its Chromophore. The Journal of Physical Chemistry B **105,** 5316–5322 (2001).
6. Genchi, L., Laptenok, S. P. & Liberale, C. Background signals in stimulated Raman scattering microscopy and current solutions to avoid them. Advances in Physics: X **8,** 2176258 (2023).
7. Camp Jr, C. H. & Cicerone, M. T. Chemically sensitive bioimaging with coherent Raman scattering. Nature Photonics **9,** 295–305 (2015).
8. Prince, R. C. & Potma, E. O. Coherent Raman scattering microscopy: capable solution in search of a larger audience. Journal of Biomedical Optics **26,** 060601 (2021).
9. Saar, B. G. et al. Video-Rate Molecular Imaging in Vivo with Stimulated Raman Scattering. Science **330,** 1368–1370 (2010).
10. Pegoraro, A. F. & Stolow, A. Chirp modulation stimulated Raman scattering microscopy. Opt. Express **32,** 31297–31310 (2024).
11. Lombardini, A. et al. Background-suppressed SRS fingerprint imaging with a fully integrated system using a single optical parametric oscillator. Opt. Express **28,** 14490–14502 (2020).
12. Freudiger, C. W. et al. Label-Free Biomedical Imaging with High Sensitivity by Stimulated Raman Scattering Microscopy. Science **322,** 1857–1861 (2008).
13. Kikuchi, K. Fundamentals of Coherent Optical Fiber Communications. Journal of Lightwave Technology **34,** 157–179 (2016).
14. Andreana, M. et al. Amplitude and polarization modulated hyperspectral Stimulated Raman Scattering Microscopy. Opt. Express **23,** 28119–28131 (2015).

15. Zhang, D., Slipchenko, M. N., Leaird, D. E., Weiner, A. M. & Cheng, J.-X. Spectrally modulated stimulated Raman scattering imaging with an angle-to-wavelength pulse shaper. Opt. Express **21,** 13864–13874 (2013).

16. Hellerer, T., Enejder, A. M. & Zumbusch, A. Spectral focusing: High spectral resolution spectroscopy with broad-bandwidth laser pulses. Applied Physics Letters **85,** 25–27. ISSN: 0003-6951 (2004).

17. Mohseni, M., Polzer, C. & Hellerer, T. Resolution of spectral focusing in coherent Raman imaging. Opt. Express **26,** 10230–10241 (2018).

18. Dhar, L., Rogers, J. A. & Nelson, K. A. Time-resolved vibrational spectroscopy in the impulsive limit. Chemical Reviews **94,** 157–193 (1994).

19. Raanan, D. et al. Sub-second hyper-spectral low-frequency vibrational imaging via impulsive Raman excitation. Opt. Lett. **44,** 5153–5156 (2019).

20. Rocha-Mendoza, I., Langbein, W. & Borri, P. Coherent anti-Stokes Raman microspectroscopy using spectral focusing with glass dispersion. Applied Physics Letters **93,** 201103. ISSN: 0003-6951 (2008).

21. Pegoraro, A. F. et al. Optimally chirped multimodal CARS microscopy based on a single Ti:sapphire oscillator. Optics Express **17,** 2984–2996. ISSN: 1094-4087 (2009).

22. Frackleton, L. et al. Fringe-averaged collinear frequency-resolved optical gating: in situ characterization of ultrashort pulses in nonlinear microscopy. Opt. Express **32,** 33090–33103 (2024).

23. Pegoraro, A. & Stolow, A. Chirp Modulation Stimulated Raman Scattering Microscopy. USPTO Patent 63,285,808 (2025).

24. Trebino, R. Frequency-Resolved Optical Gating: The Measurement of Ultrashort Laser Pulses 1st ed. (Springer-Verlag, 2000).

25. Maier, M., Kaiser, W. & Giordmaine, J. A. Intense Light Bursts in the Stimulated Raman Effect. Phys. Rev. Lett. **17,** 1275–1277 (26 1966).

26. Trebino, R. et al. Measuring ultrashort laser pulses in the time-frequency domain using frequency-resolved optical gating. Review of Scientific Instruments **68,** 3277–3295. ISSN: 0034-6748 (1997).

27. Stark, H. Image Recovery: Theory and Application eng. ISBN: 012663940X (Academic Press, Orlando, 1987).

28. DeLong, K. W., Trebino, R., Hunter, J. & White, W. E. Frequency-resolved optical gating with the use of second-harmonic generation. JOSA B **11,** 2206–2215. ISSN: 1520-8540 (1994).

29. Jafari, R., Jones, T. & Trebino, R. 100% reliable algorithm for second-harmonic-generation frequency-resolved optical gating. Opt. Express **27,** 2112–2124 (2019).

30. FROG MATLAB code available at https://frog.gatech.edu/code.html.

31. Krook, C. O. & Pasiskevicius, V. Overcoming noise in pulse retrieval: introducing the line-search FROG algorithm. Opt. Express **33,** 33258–33269 (2025).

32. Ding, F. et al. Multi-grid parallel ptychographic algorithm for frequency-resolved optical gating. Opt. Express **33,** 9117–9132 (2025).

33. Sun, H. et al. RecNet: advanced encoder-decoder architecture for SHG-FROG pulse reconstruction with enhanced noise immunity and convergence. Opt. Express **33,** 3040–3053 (2025).

34. Dudovich, N., Oron, D. & Silberberg, Y. Single-pulse coherently controlled nonlinear Raman spectroscopy and microscopy. Nature **418,** 512–514. ISSN: 1476-4687 (2002).

35. Amat-Roldán, I. et al. Ultrashort pulse characterisation with SHG collinear-FROG. Optics Express **12,** 1169–1178. ISSN: 1094-4087 (2004).

36. Stibenz, G. & Steinmeyer, G. Interferometric frequency-resolved optical gating. Optics Express **13,** 2617–2626. ISSN: 1094-4087 (2005).

37. Fittinghoff, D. N. et al. Collinear type II second-harmonic-generation frequency-resolved optical gating for use with high-numerical-aperture objectives. Optics Letters **23,** 1046–1048. ISSN: 1539-4794 (1998).

38. Fittinghoff, D. N., Millard, A. C., Squier, J. A. & Müller, M. Frequency-resolved optical gating measurement of ultrashort pulses passing through a high numerical aperture objective. IEEE Journal of Quantum Electronics **35,** 479–486. ISSN: 00189197 (1999).

39. Gallmann, L., Steinmeyer, G., Sutter, D. H., Matuschek, N. & Keller, U. Collinear type II second-harmonic-generation frequency-resolved optical gating for the characterization of sub-10-fs optical pulses. Optics Letters **25,** 269–271. ISSN: 1539-4794 (2000).

40. Sandkuijl, D., Tuer, A. E., Tokarz, D., Sipe, J. E. & Barzda, V. Numerical second- and third-harmonic generation microscopy. J. Opt. Soc. Am. B **30,** 382–395 (2013).

41. Török, P., Higdon, P. & Wilson, T. On the general properties of polarised light conventional and confocal microscopes. Optics Communications **148,** 300–315. ISSN: 0030-4018 (1998).

42. Chadwick, R. et al. Fringe-free, background-free, collinear third-harmonic generation frequency-resolved optical gating measurements for multiphoton microscopy. Optics Letters **31,** 3366–3368. ISSN: 1539-4794 (2006).

43. Hyyti, J., Escoto, E. & Steinmeyer, G. Third-harmonic interferometric frequency-resolved optical gating. JOSA B **34,** 2367–2375. ISSN: 1520-8540 (2017).

44. Galler, A. & Feurer, T. Pulse shaper assisted short laser pulse characterization. Applied Physics B: Lasers and Optics **90,** 427–430. ISSN: 09462171 (2008).

45. Sussman, B. J., Lausten, R. & Stolow, A. Focusing of light following a 4- f pulse shaper: Considerations for quantum control. Physical Review A - Atomic, Molecular, and Optical Physics **77,** 043416. ISSN: 10502947 (2008).

46. Forget, N., Crozatier, V. & Oksenhendler, T. Pulse-measurement techniques using a single amplitude and phase spectral shaper. JOSA B **27,** 742–756. ISSN: 1520-8540 (2010).

47. Wilcox, D. E., Fuller, F. D. & Ogilvie, J. P. Fast second-harmonic generation frequency-resolved optical gating using only a pulse shaper. Optics Letters **38,** 2980–2983. ISSN: 1539-4794 (2013).

48. Rullière, C., Amand, T. & Marie, X. Femtosecond Laser Pulses - Principles and Experiments 2nd ed. (Springer-Verlag, 2005).

49. Diels, J.-C. & Rudolph, W. Ultrashort laser pulse phenomena 2nd ed. eng. ISBN: 9780122154935 (Elsevier/Academic Press, 2006).

50. Available at https://www.newlightphotonics.com/Optical-Windows-Rods/SF11-Windows-Rods.

51. Connolly, J., diBenedetto, B. & Donadio, R. Specifications Of Raytran Material. https://doi.org/10.1117/12.957359 **0181,** 141–144 (1979).

52. Hyyti, J., Escoto, E., Steinmeyer, G. & Witting, T. Interferometric time-domain ptychography for ultrafast pulse characterization. Optics Letters **42,** 2185–2188. ISSN: 1539-4794 (2017).

53. Veselá, P. & Žídek, K. Influence of the delay line jitter on the SHG FROG reconstruction. Opt. Express **29,** 4392–4404 (2021).

54. Wahab, M. F. & O'Haver, T. C. Peak deconvolution with significant noise suppression and stability using a facile numerical approach in Fourier space. Chemometrics and Intelligent Laboratory Systems **235,** 104759. ISSN: 0169-7439 (2023).

55. Abdolghader, P. et al. Unsupervised hyperspectral stimulated Raman microscopy image enhancement: denoising and segmentation via one-shot deep learning. Opt. Express **29,** 34205–34219 (2021).

56. Harper, A. N., Boisvert, J., Grammatikopoulos, T., Stolow, A. & Pegoraro, A. F. Lock-in amplitude-phase correlations for enhanced imaging and segmentation in stimulated Raman scattering microscopy. Opt. Express **33,** 39406–39425 (2025).

57. Martinez, O. 3000 times grating compressor with positive group velocity dispersion: Application to fiber compensation in 1.3-1.6 µm region. IEEE Journal of Quantum Electronics **23,** 59–64 (1987).

58. Martinez, O. E., Gordon, J. P. & Fork, R. L. Negative group-velocity dispersion using refraction. J. Opt. Soc. Am. A **1,** 1003–1006 (1984).

59. Maine, P., Strickland, D., Bado, P., Pessot, M. & Mourou, G. Generation of ultrahigh peak power pulses by chirped pulse amplification. IEEE Journal of Quantum Electronics **24,** 398–403 (1988).

60. Huang, J. Ultrashort mid-infrared pulse generation in soft-glass fibre laser system Available at `https://open.fau.de/handle/openfau/14236`. PhD thesis (Friedrich-Alexander-Universität Erlangen-Nürnberg, Erlangen, DE, 2020).

61. Keller, U. in Ultrafast Lasers 73–130 (Springer International Publishing, Cham, 2021). ISBN: 978-3-030-82532-4.

62. Damask, J. N. Polarization Optics in Telecommunications 1st ed. 2005. eng. ISBN: 1-280-31196-7 (Springer New York, New York, NY, 2005).

63. Hecht, E. Optics 5 edition. eng. ISBN: 9780133977226 (Pearson Education, Inc., Boston, 2017).

64. Webb, B., Guardalben, M. J., Dorrer, C., Bucht, S. & Bromage, J. Simulation of grating compressor misalignment tolerances and mitigation strategies for chirped-pulse-amplification systems of varying bandwidths and beam sizes. Appl. Opt. **58,** 234–243 (2019).

65. Zhong, Z. et al. Investigation of Spatial Chirp Induced by Misalignments in a Parallel Grating Pair Pulse Stretcher. Applied Sciences **10.** ISSN: 2076-3417 (2020).

66. Gal, A. A. & Cagle, P. T. The 100-Year Anniversary of the Description of the Frozen Section Procedure. JAMA **294,** 3135–3137. ISSN: 0098-7484 (2005).

67. Hinton, J. P. et al. A Method to Reuse Archived H and E Stained Histology Slides for a Multiplex Protein Biomarker Analysis. Methods and Protocols **2.** ISSN: 2409-9279 (2019).

68. Chan, J. K. C. The Wonderful Colors of the Hematoxylin–Eosin Stain in Diagnostic Surgical Pathology. International Journal of Surgical Pathology **22.** PMID: 24406626, 12–32 (2014).

69. Ariotta, V. et al. H&E image analysis pipeline for quantifying morphological features. Journal of Pathology Informatics **14,** 100339. ISSN: 2153-3539 (2023).

70. Freudiger, C. W. et al. Multicolored stain-free histopathology with coherent Raman imaging. Laboratory Investigation **92,** 1492–1502 (2012).

71. Ji, M. et al. Rapid, Label-Free Detection of Brain Tumors with Stimulated Raman Scattering Microscopy. Science Translational Medicine **5,** 201ra119 (2013).

72. Lu, F.-K. et al. Label-Free Neurosurgical Pathology with Stimulated Raman Imaging. Cancer Research **76,** 3451–3462. ISSN: 0008-5472 (2016).

73. Orringer, D. A. et al. Rapid intraoperative histology of unprocessed surgical specimens via fibre-laser-based stimulated Raman scattering microscopy. Nature Biomedical Engineering **1,** 0027 (2017).

74. Appay, R. et al. Live Stimulated Raman Histology for the Near-Instant Assessment of Central Nervous System Samples. The Journal of Physical Chemistry B **127.** PMID: 37071666, 3624–3631 (2023).

75. Louis, D. N. et al. The 2021 WHO Classification of Tumors of the Central Nervous System: a summary. Neuro-Oncology **23,** 1231–1251. ISSN: 1522-8517 (2021).

76. Hou, X. et al. Intelligent Histology for Tumor Neurosurgery 2025.

77. Hollon, T. C. et al. Near real-time intraoperative brain tumor diagnosis using stimulated Raman histology and deep neural networks. Nature Medicine **26,** 52–58 (2020).

78. Akaji, S. et al. Post-staining Raman analysis of histological sections following decolorization. Analyst **147,** 4473–4479 (2022).

79. Androniem, L. et al. Raman Spectroscopy of the Hematoxylin - Eosin Stained Tissue. ProEnvironment Promediu **8,** 590–600 (2015).

80. Araujo, C. F., Nolasco, M. M., Ribeiro, A. M. & Ribeiro-Claro, P. J. Identification of microplastics using Raman spectroscopy: Latest developments and future prospects. Water Research **142,** 426–440. ISSN: 0043-1354 (2018).

81. Fang, C., Awoyemi, O. S., Luo, Y. & Naidu, R. How to Identify and Quantify Microplastics and Nanoplastics Using Raman Imaging? Analytical Chemistry **96,** 7323–7331 (2024).

82. Mansfield, J. C. et al. Label-free Chemically Specific Imaging in Planta with Stimulated Raman Scattering Microscopy. Analytical Chemistry **85,** 5055–5063 (2013).

83. Houle, M.-A. et al. Rapid 3D chemical-specific imaging of minerals using stimulated Raman scattering microscopy. Journal of Raman Spectroscopy **48,** 726–735 (2017).

84. Kao, M.-C. et al. Direct mineralogical imaging of economic ore and rock samples with multi-modal nonlinear optical microscopy. Scientific Reports **8,** 16917 (2018).